



**Convective initiation and maintenance processes of two back-building mesoscale convective systems leading to heavy precipitation events in Southern Italy during HyMeX IOP 13**

Journal:	<i>QJRMS</i>
Manuscript ID	QJ-16-0031.R1
Wiley - Manuscript type:	Research Article
Date Submitted by the Author:	28-Apr-2016
Complete List of Authors:	LEE, KEUNOK; LATMOS Site de Paris, Flamant, Cyrille; Université Pierre et Marie Curie and CNRS, LATMOS Ducrocq, Veronique; METEO-FRANCE, CNRM-GAME/GMME DUFFOURG, Fanny; CNRM-GAME, Météo-France, Fourrie, Nadia; Meteo France, CNRM GAME Davolio, Silvio; ISAC-CNR,
Keywords:	airborne water vapour lidar, AROME-WMED analyses, SEVIRI, sea surface temperature, Tyrrhenian Sea

1  
2  
3  
4 1 **Convective initiation and maintenance processes of two back-building mesoscale**  
5  
6 2 **convective systems leading to heavy precipitation events in Southern Italy during**  
7  
8  
9 3 **HyMeX IOP 13**  
10  
11

12 K.-O. Lee<sup>1†</sup>, C. Flamant<sup>1</sup>, V. Ducrocq<sup>2</sup>, F. Duffourg<sup>2</sup>, N. Fourrié<sup>2</sup>, S. Davolio<sup>3</sup>  
13  
14  
15

16 <sup>1</sup>LATMOS/IPSL, UPMC Univ. Paris 06, Sorbonne Universités, UVSQ, CNRS, Paris, France  
17

18 <sup>2</sup>CNRM-GAME, UMR 3589, Météo-France & CNRS, Toulouse, France  
19

20 <sup>3</sup>Institute of Atmospheric Sciences and Climate (CNR-ISAC), Bologna, Italy  
21  
22  
23

24  
25 11 ABSTRACT  
26

27 12 During Intensive Observation Period 13 (15–16 October 2012) of the first Special Observing Period  
28 13 of the Hydrological cycle in the Mediterranean Experiment (HyMeX), Southern Italy (SI) was  
29 14 affected by two consecutive heavy precipitation events (HPEs). Both HPEs were associated with  
30 15 multi-cell V-shaped retrograde regeneration mesoscale convective systems (MCSs). The life  
31 16 cycle of two MCSs in connection with their dynamic and thermodynamic environments were analysed  
32 17 using a combination of ground-based, airborne and spaceborne observations and numerical  
33 18 simulations. Rain gauges revealed that heavy precipitation occurred in two phases: the first one from  
34 19 1300 to 1700 UTC (35 mm h<sup>-1</sup>) was caused by a V-shaped system initiating over the Tyrrhenian Sea in  
35 20 the early morning of 15 October. Convection was triggered by the low-level convergence between the  
36 21 south-westerlies ahead of an upper-level trough positioned over south-eastern France and very moist  
37 22 southerlies from Strait of Sicily. The convection was favoured by high convective available potential  
38 23 energy (1500 J kg<sup>-1</sup>) resulting from warm and moist conditions at low levels associated with high sea  
39 24 surface temperatures in the Sicily Channel, and by the presence of an elevated moisture plume from  
40 25 tropical Africa. The second phase of heavy precipitation (2300 UTC on 15 October to 0200 UTC on  
41  
42  
43  
44  
45  
46  
47  
48  
49  
50  
51  
52  
53  
54

55  
56  
57 <sup>†</sup> Corresponding author:  
58 email: keun-ok.lee@latmos.ipsl.fr  
59  
60

16 October,  $34 \text{ mm h}^{-1}$ ) was caused by a MCS initiating over Algeria around 1300 UTC, which subsequently traveled over the Strait of Sicily toward Sicily and SI. Convection was maintained by the combination of large low-level moisture contents and elevated moisture supply associated with a tropical plume, and propagated along a marked wind shear at the leading edge of the cold front. Unlike other MCSs forming in the same region earlier on that day, this huge V-shaped system did affect SI because the strong upper-level flow progressively veered from southwesterly to south-southwesterly.

### *Running title*

*Upstream condition of deep convection over southern Italy*

### *Keywords*

*airborne water vapour lidar, AROME-WMED analyses, SEVIRI, sea surface temperature, Tyrrhenian Sea*

## **1. Introduction**

The Western Mediterranean coastal regions are frequently affected by heavy precipitation events that produce flash floods and landslides (e.g. Ricard *et al.* 2012; Llasat *et al.* 2013). The continuous formation of convection in a specific area is one of the main factors responsible for high rainfall totals. Multicell V-shaped Mesoscale Convective Systems (MCSs) with retrograde regeneration have long been studied due to their capacity to produce heavy rain in a given location (Mc Cann, 1983; Scofield, 1985; Rivrain, 1997). These meteorological phenomena result from complex multi-scale interactions between the moist ambient inflow, topography and deep convection that makes forecasting the precise timing, location and amount of the precipitation a difficult task.

In the Western Mediterranean, synoptic-scale patterns associated with heavy precipitation events (HPEs) have been shown to be connected to upper-level troughs, responsible for generating low-level marine flow characterized by high values of equivalent potential temperature and

1 precipitable water (Romero *et al.* 1999; Lin *et al.* 2001; Nuissier *et al.* 2008 and 2011; Ricard *et al.*  
2 2012). Melani *et al.* (2013) also emphasized that both upper-level tropopause dynamical anomalies  
3 and low-level intense winds play a very important role in triggering convection in coastal  
4 mountainous areas and over the sea of the western Mediterranean. The coastal mountainous region  
5 (e.g. the Pyrenees, Massif central, Alps) favours convective initiation and HPE due to enhanced  
6 orographic forcing of warm and moist low-level marine flow (Rotunno and Ferretti, 2001; Rotunno  
7 and Houze, 2007; Nuissier *et al.* 2008, 2011; Trapero *et al.* 2013a and 2013b, Barthlott and Davolio,  
8 2015); while the convective initiation over the sea is favoured by large-scale low-level convergence  
9 and flow modification around mountainous islands (e.g. Corsica, Sardinia, Balearic Islands) (Jansa *et*  
10 *al.* 2001; Coheut 2011; Barthlott *et al.* 2014; Romero *et al.* 2015). The low-level feeding flow to MCS  
11 is mostly from the south (or south-east) in southern France, but it is typically from the east or east-  
12 north-east in Spain (Catalonia, Valencia, the Balearics) and from the south-west or west in northern  
13 Italy, Corsica and Sardinia (Jansa *et al.* 2001; Romero *et al.* 1999; Nuissier *et al.* 2011). Jansa *et al.*  
14 (2001) found that about 90% of the HPEs in the Western Mediterranean involve the presence of a  
15 cyclonic centre in the vicinity, usually located so that it favours the creation and intensification of a  
16 moist low-level flow feeding the deep convection. The processes leading to moisture transport over  
17 the Mediterranean Sea are nevertheless quite diverse. Duffourg and Ducrocq (2013) estimated that  
18 evaporation from the Mediterranean accounts for only about 40% of the water vapour feeding the  
19 deep convection. The Atlantic Ocean (Winschall *et al.* 2012) and tropical Africa (Turato *et al.* 2004;  
20 Chazette *et al.* 2015b) have been also suggested as potential sources of moisture for HPEs in those  
21 regions.

22 In spite of these recent findings, the impact of the moist inflow on the timing and location of  
23 convective initiation is still poorly understood. It is also not clear that the importance of all the  
24 involved processes are well constrained. This is mainly because it is difficult to obtain relevant  
25 observations in the inflow region or within the convective storms, particularly over the sea.

26 The first Special Observation Period (SOP1, Ducrocq *et al.* 2014) of the Hydrological cycle in  
27 the Mediterranean Experiment (HyMeX, <http://www.hymex.org/>; Drobinski *et al.* 2014), took place

1  
2  
3  
4 1 in Autumn 2012 (from 5 September to 6 November). It aimed to improve our knowledge of the origin  
5  
6 2 and transport pattern of moist air masses in pre-convective conditions and determine the link between  
7  
8 3 these air masses and HPEs. During SOP1, dedicated ground-based, airborne and sea-borne observing  
9  
10 4 platforms were operated with the objective of documenting the connection between the moist flow  
11  
12 5 over the Mediterranean and HPEs occurring over the coastal areas of Spain, France and Italy.

14 Our study focuses on two HPEs over southern Italy (SI) and the associated inflow from over the  
15  
16 7 Tyrrhenian Sea. This is one of the preferential area for deep convection development in fall (Melani *et*  
17  
18 8 *al.* 2013) and these events occurred during the Intensive Observation Period 13 (IOP 13, 15–16  
19  
20 9 October 2012). The HPEs were associated with the south-eastward movement of a cold front from  
21  
22 10 southern France to SI which led to intense rainfall (Fig. 1). Behind the cold front, mistral winds  
23  
24 11 prevailed bringing cold and dry continental air over the sea. The mistral is frequently observed to  
25  
26 12 extend as far as a few hundred kilometres from the coast and is one of the primary causes of storms  
27  
28 13 over the Mediterranean (Jansa, 1987; Trigo *et al.* 1999; Campins *et al.* 2000; Drobinski *et al.* 2005; Di  
29  
30 14 Girolamo *et al.* 2016). In the frontal region, the potential vorticity anomaly associated with the upper-  
31  
32 15 level trough was responsible for the development of deep convection and intense rainfall over central  
33  
34 16 Italy during IOP 13 (Barthlott and Davolio, 2015). In the early morning of 15 October, intense  
35  
36 17 rainfalls (60–80 mm) was observed near the Liguria coast and in Tuscany (Fig. 1a). In the Liguria  
37  
38 18 coast region, associated with the warm sector of the approaching frontal system, orographic blocking  
39  
40 19 and uplift of low-level southerly flow triggered the development of heavy rainfall. Later on, a locally-  
41  
42 20 generated low-level convergence in the lee of Corsica contributed to generate heavy rainfall in the  
43  
44 21 Tuscany region (for details, see Barthlott and Davolio, 2015). Subsequently, as the cold front moved  
45  
46 22 southward, SI experienced two periods of intense rainfall, peaking at 1700 UTC on 15 October  
47  
48 23 (maximum rainfall intensity of 34.8 mm h<sup>-1</sup>), and at 0100 UTC on 16 October (33.8 mm h<sup>-1</sup>). The  
49  
50 24 MCSs developing over the Tyrrhenian Sea and the Strait of Sicily were successfully captured by  
51  
52 25 ground-based, airborne and spaceborne observations. Furthermore, Rysman *et al.* (2015) reported that  
53  
54 26 deep convection frequency during IOP 13 was between 2 to 4 times larger than the average for the  
55  
56 27 period 2000–2013 and this period included particularly large MCSs travelling from Tunisia to Italy.

1  
2  
3  
4 1 Funatsu *et al.* (2009) also used spaceborne observations from the Advanced Microwave Sounding  
5  
6 2 Unit radiometer to show the existence of an autumnal convective arc between Tunisia and SI during  
7  
8 3 the period of 2001-2007. Even though these climatological analyses using the long-term satellite data  
9  
10 4 have highlighted the high frequency of MCSs in this area upstream of SI, process oriented case  
11  
12 5 studies allowing investigations of convective initiation and maintenance in connection with the  
13  
14 6 dynamic and thermodynamic environment have not been conducted up to now.

15  
16 7 The aim of the present study is to conduct such a detailed investigation using the wealth of data  
17  
18 8 acquired off-shore and inland during IOP 13, together with analyses from the numerical weather  
19  
20 9 prediction (NWP) model AROME-WMED (Application of Research to Operations at Mesoscale-  
21  
22 10 West Mediterranean, Fourrié *et al.* 2015).

23  
24 11 A detailed description of the dataset is presented in Section 2. Section 3 provides an overview  
25  
26 12 of the two HPEs that occurred over SI during IOP 13 of the HyMeX SOP 1. Sections 4 and 5 detail  
27  
28 13 the HPEs over SI during P1 and P2 respectively, including the life cycle of the MCSs and mesoscale  
29  
30 14 environmental dynamics and thermodynamics. A summary and a discussion of the findings of the  
31  
32 15 present study are given in Section 6.

33  
34 16

## 35 36 17 **2. Observational and modelling dataset**

37  
38 18 Unprecedented samplings of the dynamic and thermodynamic environment of HPEs in the western  
39  
40 19 Mediterranean region was achieved during the HyMeX SOP1 (Ducrocq *et al.* 2014). More details  
41  
42 20 concerning the observational datasets used in this study and the AROME-WMED analysis data are  
43  
44 21 provided in the following.

45  
46 22

### 47 48 23 **2.1. HyMeX SOP1 observational dataset**

#### 49 50 24 **2.1.1. Existing and enhanced surface networks**

51  
52 25 Hourly and 24-h accumulated rainfall (version V2) data over the HyMeX domain (western  
53  
54 26 Mediterranean basin) were used, and the locations of the surface rain gauges over France and Italy  
55  
56 27 used in this study are shown in Fig. 1. In addition, hourly surface station (SYNOP) data were

1 employed to show the near-surface (2 m) temperature field. Data from radiosondes launched in  
2 Trapani (western Sicily, 12.3°E, 37.5°N) were also exploited (see Fig. 1b for location). Hourly  
3 horizontal distribution of total integrated water vapour (TIWV) content was derived from a network  
4 of global positioning system (GPS) stations (Bock *et al.* 2015). In addition, we used the half-hourly  
5 buoy measurements (www.coriolis.eu.org) of the sea surface temperature (SST) in the Strait of Sicily  
6 (around 11.5°E, 37.5°N; a star symbol in Fig. 1b). Finally, lightning data from the ZEUS system  
7 operated by the National Observatory of Athens was used to identify the most active convective  
8 clouds. ZEUS is a long-range lightning detection network (Kotroni and Lagouvardos, 2008) with  
9 receivers located at six sites over Europe (Birmingham in the UK, Roskilde in Denmark, Iasi in  
10 Romania, Larnaka in Cyprus, Mazagon in Spain, and Athens in Greece).

#### 11 12 *2.1.2. Dedicated HyMeX SOP 1 airborne observations*

13 The LEANDRE 2 water vapour lidar on-board the SAFIRE (Service des Avions Français  
14 Instrumentés pour la Recherche en Environnement) ATR42 aircraft sampled the low-level moisture in  
15 the environment of the convective systems, which developed during the IOP 13 (ATR42 flight AS 49).  
16 The ATR42 flew back and forth between Bastia (Corsica, France) and Palermo (Sicily, Italy) from  
17 0747 UTC to 1059 UTC on 15 October 2012. The LEANDRE 2 characteristics allowed  
18 measurements of the water vapour mixing ratio (WVMR) profiles with a precision ranging from less  
19 than 0.1 g kg<sup>-1</sup> at 4.5 km above ground level to less than 0.4 g kg<sup>-1</sup> near the surface (on average) for an  
20 along-beam resolution of 150 m (for the details, see Bruneau *et al.* 2001a and 2001b). During HyMeX  
21 SOP 1, WVMR profiles were measured with a horizontal resolution of 1 km (e.g. Chazette *et al.*  
22 2015a, 2015b; Di Girolamo *et al.* 2016; Duffourg *et al.* 2015; Flamant *et al.* 2015; Flaounas *et al.*  
23 2015).

#### 24 25 *2.1.3. Spaceborne observations*

26 Calibrated thermal infrared brightness temperature (BT) data at 10.8 μm and 6.2 μm, acquired every 5  
27 min by the Spinning Enhanced Visible and Infrared Imager (SEVIRI) on-board the geostationary

1  
2  
3  
4 1 Meteosat Second Generation satellite (MSG, Bedka, 2011) were employed to investigate the evolution  
5  
6 2 of deep convection. The spatial resolution of the MSG-SEVIRI data used is  $0.05^\circ$  in both latitude and  
7  
8 3 longitude. The deep convective systems leading to heavy precipitation in the SI domain were  
9  
10 4 identified using SEVIRI BT at  $10.8\ \mu\text{m}$  together with lightning activity. BT minima are generally  
11  
12 5 indicative of the cloud top overshoots associated with deep convection (e.g. Kato, 2006; Bedka, 2011).  
13  
14 6 As suggested by Kato (2006) a threshold value of 220 K was used in this analysis to identify deep  
15  
16 7 convective cells, causing heavy precipitation. BTs at  $6.2\ \mu\text{m}$  (the so-called water vapour channel)  
17  
18 8 were utilised to characterize the distribution of moisture in the upper troposphere at the mesoscale.  
19  
20 9 BTs higher than  $-40^\circ\text{C}$  (lower than  $-50^\circ\text{C}$ ) are generally considered as representative of dry (moist)  
21  
22 10 upper-level air masses (Setvák *et al.* 2007; Bedka *et al.* 2009).  
23

24  
25 11 The National Oceanic and Atmospheric Administration (NOAA) oceansat-2 scatterometer  
26  
27 12 (OSCAT, <http://manati.star.nesdis.noaa.gov/products/OSCAT.php>) ocean surface wind vector  
28  
29 13 retrievals (level 2) at a spatial resolution of 25-km are employed to reveal the 10-m wind fields over  
30  
31 14 the Western Mediterranean on 15 October. OSCAT overpassed the Western Mediterranean region  
32  
33 15 twice on 15 October: around 1130 UTC during the descending-orbit (crossing  $35^\circ\text{N}$  at 1135 UTC) and  
34  
35 16 around 2230 UTC during the ascending-orbit (crossing  $35^\circ\text{N}$  at 2230 UTC).  
36

37  
38 17 The moisture retrievals obtained from the Moderate Resolution Imaging Spectro-radiometer  
39  
40 18 (MODIS) on-board the TERRA satellite were also employed (<http://gdata1.sci.gsfc.nasa.gov/>). The  
41  
42 19 MODIS-derived TIWV contents and the partial integrated water vapour (PIWV) column between  
43  
44 20  $700\text{-hPa}$  and  $300\ \text{hPa}$  levels were analysed in order to describe the distribution of moisture at the  
45  
46 21 synoptic scale during the events.

47  
48 22 To investigate the impact of SST variability on the atmospheric moisture content and  
49  
50 23 convective initiation, the Météo-France Centre for Satellite Meteorology multisensor SST analysis  
51  
52 24 data were used. These data are obtained by an optimal interpolation of supercollated multi-sensor  
53  
54 25 level 3 merged SST. The spatial resolution is  $0.02^\circ$  in both latitude and longitude, and the temporal  
55  
56 26 resolution is 3 h. Observations from SEVIRI on MSG, MODIS on TERRA satellites, from the  
57  
58 27 Advanced Very High Resolution Radiometer on the Meteorological Operational Satellite Program of  
59  
60



1 Europe and the NOAA platforms as well as the Advanced Along-Track Scanning Radiometer on the  
2 Environmental Satellite were used to produce the SST analysis (Cailleau *et al.* 2012).

## 3 4 **2.2. The NWP model AROME-WMED**

5 To support the field campaign activities and to optimize flight planning during SOP1, a dedicated  
6 version of the operational convection permitting NWP model AROME was implemented (Fourrié *et*  
7 *al.* 2015). AROME-WMED is a regional non-hydrostatic, and fully-compressible and convection  
8 permitting model, covering the western Mediterranean basin with 2.5 km horizontal resolution and 60  
9 vertical levels ranging from 10 m above ground to 1 hPa.

10 AROME-WMED implements the surface scheme (SURFEX; Masson *et al.* 2013) which  
11 diagnoses the 2 m temperature, 2 m humidity, and 10 m wind at every time step through a specific  
12 algorithm called surface boundary layer (Masson and Seity, 2009). Further model details can be found  
13 in Seity *et al.* (2011). The lateral boundary conditions are updated hourly and provided by the French  
14 operational global model Action de Recherche Petite Echelle Grande Echelle (ARPEGE, Courtier *et*  
15 *al.* 1991) forecasts.

16 With 3-h cycles, the initial atmospheric state of the AROME-WMED analyses is performed  
17 with the AROME data assimilation system (Brousseau *et al.* 2008) which is derived from the regional  
18 Aire Limitée Adaptation Dynamique Développement International (ALADIN)-France 3D-Var scheme.  
19 At a 2.5 km horizontal resolution, AROME assimilates data from radiosondes, wind profilers, ships  
20 and buoys, surface stations (i.e. pressure, 2-m temperature and humidity, 10-m wind), GPS stations  
21 (i.e. TIWV), radars (i.e. radar-derived winds) and SEVIRI (i.e. infrared radiances) (Seity *et al.* 2011).  
22 Many important observing systems, such as SYNOPs, radar and SEVIRI data, are assimilated at a  
23 high frequency. An optimal interpolation scheme is conducted.

24 Fourrié *et al.* (2015) showed that the overall performances of the AROME-WMED were good  
25 for the HyMeX SOP1 (mean 2-m temperature root mean square error (*RMSE*) of  $\sim 1.7^{\circ}\text{C}$  and mean 2-  
26 m relative humidity *RMSE* of  $\sim 10\%$ ) and similar to those of the AROME-France for the 0–30 h  
27 common forecast range (maximal absolute difference of the 2-m temperature *RMSE* of  $0.2^{\circ}\text{C}$  and  $\sim 0.2\%$

1 for the 2-m relative humidity). Bock *et al.* (2015) highlighted a very good TIWV agreement between  
2 the AROME-WMED analyses products and GPS-observations, with a small wet bias in the models  
3 ( $\sim 0.3 \text{ kg m}^{-2}$ ) and a standard deviation of differences of  $\sim 1.6 \text{ kg m}^{-2}$ . Chazette *et al.* (2015a) found  
4 good agreement between the TIWVs derived from AROME-WMED forecast and the Water vapour  
5 and Aerosol Lidar (WALI) during the entire SOP 1 (bias of  $\sim 1 \text{ kg m}^{-2}$  and *RMSE* of  $\sim 2 \text{ kg m}^{-2}$ ). They  
6 also showed that the AROME-WMED forecast and WALI water vapour mixing ratio profiles in the  
7 lower troposphere (below 6 km amsl) exhibited biases less than  $1 \text{ g kg}^{-1}$ .

8 In the present study, the AROME-WMED analyses data provided every 3 hours are used  
9 together with observations to enhance our understanding of processes responsible for HPEs in SI.

### 10 11 **3. HPEs over southern Italy**

12 During 15–16 October 2012 (IOP 13), the SI area (Fig. 1) was affected by two HPEs. At 1200 UTC  
13 on 15 October, an upper-level trough was located over south-eastern France, extending to northern  
14 Algeria (Fig. 2a). Later it moved eastwards towards Corsica. Ahead of the trough, at 500 hPa levels,  
15 south-westerly winds stronger than  $20 \text{ m s}^{-1}$  prevailed over the Tyrrhenian Sea and SI. At lower levels  
16 (Fig. 2b), the cold front shifted over the Mediterranean Sea, and undulated around a low pressure  
17 centre situated close to the Gulf of Genoa at 1200 UTC. Behind the front, cold air was present at  
18 every level; ahead of the front, the flow was south-westerly and rather intense at every level. Details  
19 about the synoptic situation during this IOP can be found in Barthlott and Davolio (2015).

20 The temporal evolution of the maximum hourly rainfall recorded by the rain gauge network  
21 during IOP 13 in the SI domain is shown in Fig. 3. The first intense rainfall period (**P1**), defined as  
22 maximum precipitation exceeding of  $10 \text{ mm h}^{-1}$ , occurred between 1300–1700 UTC on 15 October  
23 (total precipitation of 62.4 mm), and a maximum rainfall intensity of  $34.8 \text{ mm h}^{-1}$  was recorded  
24 between 1600–1700 UTC. The second intense rainfall period (**P2**) occurred from 2300 UTC on 15  
25 October to 0200 UTC on 16 October (total precipitation of 75 mm), with a maximum rainfall intensity  
26 of  $33.8 \text{ mm h}^{-1}$  between 0000–0100 UTC. During IOP 13, the highest GPS-derived TIWV values  
27 ( $\sim 33.5 \text{ kg m}^{-2}$ ) were recorded by a station located at  $15.8^\circ\text{E}$ ,  $39.9^\circ\text{N}$  at 0000 UTC on 16 October. The

1 hourly TIWV at this station (Fig. 3) shows that the TIWV values were continuously in excess of 25 kg  
2 m<sup>-2</sup> from 1000 UTC, 15 October to 0300 UTC, 16 October.

3 The hourly evolution of the BT and lightning activity during **P1**, from 1300 UTC to 1600 UTC  
4 on 15 October, is shown in Fig. 4. During this period, the SI domain was affected by a V-shaped MCS  
5 (referred to as MCS A in the following) which has formed over the Tyrrhenian Sea. The MCS was  
6 initiated in the northern part of the Strait of Sicily around 11.5°E/38°N at 0245 UTC and developed  
7 into a V-shaped multi-cell retrograde regeneration convective system at around 0400 UTC (not  
8 shown). It then drifted north-eastward when it reached 12.5°E/39°N at 1300 UTC. At the apex of the  
9 V-shaped MCS, the strongest convective cells were associated with a BT minima of 208 K (cloud top  
10 height ~13 km) and strong lightning activity. Behind the overshooting cloud at the apex, a region of  
11 higher BT ( $\leq 220$  K, cloud top height ~10 km) extended north-eastward, from the area over the sea  
12 where new convective cells formed to the SI domain, with the mid-level south-westerly flow.  
13 Subsequently, from 1400 UTC to 1600 UTC (Fig. 4b–d), the convective part of MCS A (as diagnosed  
14 from lightning activity) and its anvil (characterized by BT  $\leq 220$  K) moved north-eastward, over the  
15 SI area. At 1600 UTC, a core of lightning activity was observed inland, close to the coast indicating  
16 intense convective cells over the SI domain, responsible for heavy precipitation as shown in Fig. 3.  
17 After 1800 UTC, the low BT region progressively disappeared (not shown).

18 The hourly evolution of the BT and lightning activity from 2200 UTC to 0100 UTC during **P2**  
19 is shown in Fig. 5. At 2200 UTC (Fig. 5a), a huge V-shaped MCS cluster (referred to as MCS B in the  
20 following) was observed over Sicily. The most intense convection was observed at the apex of the  
21 MCS over the southern of Sicily and was characterized by very-low BT values (~202 K, cloud top  
22 height ~14 km) and strong lightning activity. Leeward of this minimum BT region, warmer cloud with  
23 BTs of 210–220 K (cloud top height ~13 km) covered a large domain (12–17°E/36–40.5°N),  
24 extending north-eastward from the convective core, towards SI with the mid-level south-westerly flow.

25 The storm initiated over elevated terrain in the region of Batna (Algeria) around 1330 UTC (Fig.  
26 4b-d). Orographic forcing associated with the highest summit in that region (i.e. Djebel Chélia,  
27 peaking at 2328 m amsl) likely was the cause of convective initiation. Two other convective systems

1 formed close to Tunisia before MCS B but they did not affect the SI region. MCS I developed  
2 offshore of Tunisia at 0600 UTC (visible at 0930 UTC in Fig. 6) and MCS II over Tunisia at 1000  
3 UTC (visible at 1300 UTC in Fig. 4a). Both MCSs dissipated before reaching continental Italy. Unlike  
4 MCS I and MCS II, MCS B was guided toward SI as the strong flow ahead of the trough  
5 progressively veered from southwesterly to south-south-westerly.

6 At 2300 UTC (Fig. 5b), the most active part of the MCS B ( $BTs \leq 210$  K and lightning activity)  
7 was observed over the southern part of Sicily (near  $15^{\circ}E/37^{\circ}N$ ). The large MCS anvil (characterized  
8 by BT values less than 220 K) extended northward, reaching the SI area. Later, MCS B travelled  
9 north-eastward with a convective core positioned over the Strait of Messina (between Sicily and  
10 continental Italy) at 0000 UTC on 16 October (Fig. 5c), and over Calabria at 0100 UTC (Fig. 5d),  
11 thereby approaching the SI area. This period corresponds with the time during which intense hourly-  
12 rainfall was recorded by rain gauges (Fig. 3). The most active part of MCS B was located over the  
13 southern part of Sicily. Hence, during P2, the observed rainfall is likely related to the stratiform part  
14 of MCS B rather than its convective core. It could also be related to orography-forced convection as  
15 the south-westerly flow ahead of the front impinges on the SI orography. Due to MCS B's widespread  
16 anvil and the lack of adequate instrumentation (i.e. radars), neither the convectively-forced convection  
17 nor the stratiform clouds associated with MCS B could be observed. It is therefore not clear what  
18 fraction of rainfall during P2 is provided by each of the two processes described above.

19 After 0300 UTC,  $10.8 \mu m$  BTs less than 220 K were scarce over SI in the SEVIRI imagery (not  
20 shown) as severe weather moved north-eastward.

## 21

## 22 **4. Environmental characteristics of MCS A**

### 23 **4.1. Observations**

24 The OSCAT-retrieved surface wind field (Fig. 4a) shows three distinct regions with different wind  
25 components during P1: 1) a region with north-westerly mistral winds ( $\geq 10 \text{ m s}^{-1}$ ) behind the cold  
26 front extending from the Gulf of Lion to 150 km north of the Algerian coastline, 2) a region with  
27 weak westerly to south-westerly winds ( $3\text{--}7 \text{ m s}^{-1}$ ) ahead of the front along the northern coastlines of

1  
2  
3  
4 1 Algeria and Tunisia and over the Tyrrhenian Sea, and 3) a region with moderate south-easterly winds  
5  
6 2 ( $5\text{--}10\text{ m s}^{-1}$ ) over the Strait of Sicily and downstream of the Strait of Messina. Over the southern  
7  
8 3 Tyrrhenian Sea ( $13^{\circ}\text{E}$ ,  $38.5^{\circ}\text{N}$ ), the weak westerly ( $\leq 5\text{ m s}^{-1}$ ) and the moderate south-easterly winds  
9  
10 4 ( $\sim 10\text{ m s}^{-1}$ ) converged. Meanwhile, along the western coast of Sicily, the moderate south-easterlies  
11  
12 5 ( $5\text{--}10\text{ m s}^{-1}$ ) over the Sicily Channel abruptly turned to south-westerly around the northern tip of the  
13  
14 6 island (Fig. 4a), converging with the weak westerlies (about  $11^{\circ}\text{E}$ ,  $38^{\circ}\text{N}$ ), where the MCS B  
15  
16 7 developed.

17  
18 8 Over the Tyrrhenian Sea, where the surface south-westerlies ( $3\text{--}7\text{ m s}^{-1}$ ) were captured by  
19  
20 9 OSCAT (Fig. 4a), the daily composite of the MODIS (Fig. 7a) shows high values of TIWV between  
21  
22 10  $30\text{--}35\text{ kg m}^{-2}$  (in agreement with TIWV computed from the radiosonde in Trapani that was  $\sim 31\text{ kg m}^{-2}$   
23  
24 11  $^2$  at 1200 UTC). About 75 % of the TIWV (about  $23\text{--}26\text{ kg m}^{-2}$ ) was distributed between surface and  
25  
26 12 700 hPa (not shown). Even higher TIWVs ( $35\text{--}40\text{ kg m}^{-2}$ ) were attained over the Strait of Sicily  
27  
28 13 where south-southwesterly winds ( $5\text{--}10\text{ m s}^{-1}$ ) at the surface (Fig. 4a) were observed by OSCAT.  
29  
30 14 Conversely, the mistral wind region was characterized by low TIWVs ( $\leq 20\text{ kg m}^{-2}$ ).

31  
32 15 These large TIWV values over the Strait of Sicily were associated with an elevated moist plume  
33  
34 16 coming from tropical Africa as shown by the PIWV composite (Fig. 7b). The south-west to north-east  
35  
36 17 elongated moist filament was characterized by PIWV values between 7 and  $15\text{ kg m}^{-2}$ . High PIWV  
37  
38 18 values ( $7\text{--}11\text{ kg m}^{-2}$ ) were observed with MODIS in the vicinity of MCSs A and B. Similar features  
39  
40 19 have been identified by Chazette *et al.* (2015b) for another HPE over the Cévennes during IOP 15b.  
41  
42 20 As in Chazette *et al.* (2015b), the elevated moist filament was associated with strong south-westerlies  
43  
44 21 ( $25\text{--}30\text{ m s}^{-1}$ ) at 700 hPa level (not shown) ahead of a pronounced trough positioned over Eastern  
45  
46 22 France. In our case, elevated moisture may have strengthened the updrafts associated with the V-  
47  
48 23 shaped MCS A once deep convection was initiated.

49  
50 24 More details on the vertical structure of the moisture field are provided by LEANDRE 2-  
51  
52 25 derived WVMR observations. Figure 6 shows the ATR flight track (black line) together with the BT  
53  
54 26 observed at  $6.2\text{ }\mu\text{m}$  with SEVIRI at the time when the ATR was flying closest to MCS A ( $\sim 0930\text{ UTC}$ ).  
55  
56 27 The vertical structure of the moisture field upstream of the MCS was characterized using LEANDRE  
57  
58  
59  
60

1  
2  
3  
4 1 2-derived WVMR observations (Fig. 8a) where three distinct layers with different WVMR  
5  
6 2 characteristics can be identified. A moist marine atmospheric boundary layer (MABL) with WVMRs  
7  
8 3 on the order of 10-12 g kg<sup>-1</sup> was seen to deepen from ~600 m amsl offshore of Corsica to almost 2000  
9  
10 4 m amsl in the vicinity of MCS A (located around 39°N, see the star in Fig. 8a). Low-level moisture is  
11  
12 5 one of the main ingredients of the mesoscale environment enabling heavy precipitation (Ricard *et al.*  
13  
14 6 2012). Moreover, the low-level moisture seen in Fig. 6a in the region of MCS A possibly contributed  
15  
16 7 to increase the CAPE in the region of interest over the Tyrrhenian Sea, thereby producing larger storms  
17  
18 8 with stronger peak updrafts and low-level downdrafts and heavier precipitation (Lerach and Cotton,  
19  
20 9 2012).

21  
22 10 Another striking feature observed was the very dry layer (WVMR less than ~2 g kg<sup>-1</sup>) north of  
23  
24 11 MCS A, whose base was slopping from ~5 km amsl at 41.7°N to about 2 km amsl in the vicinity of  
25  
26 12 the MCS. This dry elevated layer was also observed to thin out towards the south. Back-trajectory  
27  
28 13 analyses (not shown) suggest that this dry air was associated with air masses from the Atlantic Ocean,  
29  
30 14 subsiding from the upper troposphere ahead of the upper-level trough. LEANDRE 2 backscatter  
31  
32 15 measurement indicated that this dry layer was also very clean (i.e. aerosol-free, not shown). This dry  
33  
34 16 feature corresponds to the stripe of elevated 6.2 μm BTs observed in Fig. 7 extending from southern  
35  
36 17 Sardinia to central Italy. The structure and origin of the dry layer in the vicinity of MCS A suggests  
37  
38 18 that the cold front has the characteristics of a kata-front (Browning, 1986), and possibly contributed to  
39  
40 19 prolong the lifetime of the MCS.

41  
42 20 Between the MABL and the dry air aloft, LEANDRE 2 revealed the presence of a layer with  
43  
44 21 intermediate WVMR values (~5 g kg<sup>-1</sup>). It is worth noting that most of the isolated clouds observed  
45  
46 22 by lidar north of MCS A (e.g. around 41.3°N or 40.1°N) extended up to the top of the intermediate  
47  
48 23 layer, just below the dry layer. Finally, upstream of MCS A, the lower troposphere above MABL was  
49  
50 24 observed to be moister than immediately north of MCS A by as much as 3-4 g kg<sup>-1</sup> between 2-4 km  
51  
52 25 amsl.

53  
54  
55 26 In addition to the dry feature observed over the Tyrrhenian Sea described above, it is also worth  
56  
57 27 noting the region of high BTs (drier upper-level troposphere) in the western part of the domain in Fig.

1 7, which was associated with the upper-level trough positioned over eastern France. The largest BTs  
2 are observed over the Gulf of Lion where the dry wind is blowing from the continent. A well-defined  
3 gradient on 6.2  $\mu\text{m}$  BT is observed over the sea. Those high BT values corresponding to dry, cloud-  
4 free upper-level air masses (high BT values at 10.8  $\mu\text{m}$  in Fig. 4) were observed to move eastward  
5 between 1300–1600 UTC (Fig. 4).

#### 6 7 **4.2. AROME-WMED analyses**

8 Over the southern Tyrrhenian Sea, a region of high TIWV ( $\geq 35 \text{ kg m}^{-2}$ , Fig. 9a) and high CAPE  
9 (larger than 1500  $\text{J kg}^{-1}$ , red contour line in Fig. 9c) is seen in the AROME-WMED analyses at 1200  
10 UTC around 13°E/39°N, i.e. where the V-shaped MCS A described above was observed. The high  
11 TIWVs (35–40  $\text{kg m}^{-2}$ ) over the southern Tyrrhenian Sea and the Strait of Sicily were in agreement  
12 with the MODIS-derived TIWVs (Fig. 7a). A good agreement between AROME-WMED and  
13 LEANDRE 2 observations is found above the MABL, between 2–4 km amsl (see Fig. 8c–d), while  
14 some relatively large differences can be seen in the lower troposphere in the area just upstream of the  
15 MCS. Here the lowest 1000 m of the atmosphere appears too moist in the AROME-WMED  
16 simulation with respect to the observations, by about 3–4  $\text{g kg}^{-1}$  (Fig. 8d). This error can possibly be  
17 ascribed to the presence of clouds causing biases in the water vapour measurements in that region.

18 Consistent with OSCAT observations (Fig. 4), the strong convergence between south-westerlies  
19 and southerlies winds ( $6\text{--}8 \times 10^{-4} \text{ s}^{-1}$ ) is depicted over the southern Tyrrhenian Sea and over the  
20 northern Sicily Strait in the AROME-WMED analyses (Fig. 9b). Furthermore, the mistral flow behind  
21 the cold front is also reproduced in the AROME-WMED analyses at 1200 UTC and is characterised  
22 by dry air masses ( $\text{TIWV} \leq 20 \text{ kg m}^{-2}$ , Fig. 9a), strong north-westerly winds at 925 hPa ( $\sim 20 \text{ m s}^{-1}$ ,  
23 Fig. 9b) and low 2-m temperatures (less than 19°C, Fig. 9c). Over this region, low wet-bulb potential  
24 temperatures ( $\theta_w \leq 280 \text{ K}$ , Fig. 9d) were simulated at 850 hPa and intense south-westerlies prevailed  
25 at 500 hPa level. The leading edge of the mistral forms an arc spanning from 4°E/38°N to 11°E/44°N  
26 with a marked convergence (Fig. 9b) along the between of the geopotential iso-contours of 5480m and  
27 5520 m, and higher  $\theta_w$  of 285–290 K (Fig. 9d).

1  
2  
3  
4 1 In this favourable environment, MCS A develops ahead of the cold front in correspondence  
5  
6 2 with the high temperature and large moisture contents from the Sicily Channel and low-level  
7  
8 3 convergence caused by the confluence of the weak westerlies in the south Tyrrhenian Sea ahead of the  
9  
10 4 frontal region and the south-westerly flow with the large CAPE. The triggered narrow V-shape MCS  
11  
12 5 A lasted for many hours over the southern Tyrrhenian Sea propagating toward the SI together with the  
13  
14 6 south-eastward moving front.  
15  
16 7

## 18 **5. Environmental characteristic of MCS B**

19  
20 9 MCS I, II and B crossed a region of strong SST gradient in the Strait of Sicily, around the buoy  
21  
22 10 location (Fig. 10a). High SSTs on the order of 27°C prevailed to the south of the Sicily Channel, while  
23  
24 11 SSTs around 23°C were observed in the vicinity of the buoy (around 11.5°E, 37.5°N, Fig. 10a–b).  
25  
26 12 The storm track of MCSs I, II and B and the BT signature of the three MCSs at the location of the  
27  
28 13 buoy can be seen in Fig. 10b. The SST measured by the buoy was 23.2°C during most of 14 October  
29  
30 14 and the morning of 15 October indicating no change caused by the passage of MCS I (Fig. 9b). No  
31  
32 15 precipitation associated with MCS I was recorded by the rain gauge closest to the location of the buoy  
33  
34 16 in the western part of Sicily (~95 km away, circle in Fig. 10; 12.5°E, 38°N). Around 12 UTC on 15  
35  
36 17 October, SST dropped to 23.1°C, simultaneously with the passage of MCS II. This was likely due to  
37  
38 18 surface cooling by rain (rainfall was observed over Sicily ~4 h after the minimum of 10.8  $\mu\text{m}$  BT  
39  
40 19 observed at the location of the buoy).  
41  
42 20

43 20 Subsequently, the SST further dropped to 22.9°C, concomitant to the passage of MCS B around  
44  
45 21 1600 UTC. Here again the cooling was probably associated with precipitation, since rainfall was  
46  
47 22 observed ~4 h later over western Sicily. Greater rainfall amounts associated with MCS B (i.e.  
48  
49 23 maximum of 17 mm h<sup>-1</sup> at 2100 UTC) may also explain the stronger cooling (i.e. 0.2°C) than that  
50  
51 24 associated with MCS II (0.1°C for the maximum rainfall of 6 mm h<sup>-1</sup>). Finally, after the passage of  
52  
53 25 MCS B over the buoy (i.e. after 1800 UTC), 10.8  $\mu\text{m}$  BTs were observed to be on the order of 285 K,  
54  
55 26 revealing the absence of deep convection, as the dry air mass associated with the upper-level trough  
56  
57 27 moved over this area.  
58  
59  
60



1  
2  
3  
4 1 At 2100 UTC, MCS B was located just east of the eastward-moving upper-level trough (as  
5 revealed from SEVIRI 6.2  $\mu\text{m}$  BTs, Fig. 11a) and the associated low-level cold front. The position of  
6 the BT arc-shaped feature coincides with the 10  $\text{kg m}^{-2}$  iso-contour in the TIWV field displayed by the  
7 AROME-WMED analysis (Fig. 12a). MCS B was located in a moist environment east of this iso-  
8 contour characterized by the TIWV values in excess of 35  $\text{kg m}^{-2}$ . This elongated feature of the  
9 humidity field was associated with the tropical moist plume previously identified (TIWV in Trapani  
10 reached 30  $\text{kg m}^{-2}$ ).

11  
12 8 During P2, OSCAT (Fig. 5a) showed that the mistral reached northern Africa and penetrated  
13 over the Strait of Sicily while being accelerated by channelling between Sicily and Tunisia.  
14 Meanwhile, the northerlies converged with the frontal westerlies (5–10  $\text{m s}^{-1}$ ) to the north and south  
15 of MCS B ahead of the mistral.

16  
17 12 At higher levels (500 hPa), strong south-westerlies ( $\sim 30 \text{ m s}^{-1}$ ) prevailed ahead of the cold front  
18 and upstream of the SI area (Fig. 12d), while the mistral area was topped by strong north-westerlies  
19 ( $\sim 25 \text{ m s}^{-1}$ ). The warm  $\theta_w$  ( $\geq 290 \text{ K}$ ) at 850 hPa, between geopotential iso-contours of 5560m and  
20 5640 m, appeared to be associated with the front. Ahead of the front, a broad region characterized by  
21 strong low-level convergence ( $8.5 \times 10^{-4} \text{ s}^{-1}$ ) was identified by AROME-WMED (Fig. 12b).  
22 Simultaneously, warm air temperatures ( $\geq 24^\circ\text{C}$ ) as well as a fairly small area of high CAPE ( $\geq 1000 \text{ J}$   
23  $\text{kg}^{-1}$ , black contour line in Fig. 12c) were displayed upstream of the MCS B. The high CAPE region  
24 previously observed over Tunisia at 1200 UTC (Fig. 9c) has moved offshore at 2100 UTC (Fig. 12c),  
25 south of Sicily. This was likely related to the progression of the dry low-level mistral flow, which  
26 reached the Strait of Sicily at 2100 UTC (Fig. 12b).

27  
28 22 These favourable environmental condition determined by the combination of strong frontal  
29 wind shear in the Strait of Sicily, large low-level moisture contents, elevated moisture supply, warm  
30 SST, and high air temperature enabled the maintenance of the huge V-shape MCS B over the Strait of  
31 Sicily. Furthermore, we also acknowledge the fact that the cold front and/or the upwards forcing  
32 associated to the advancing branch of the upper level trough could have been important factors in the  
33 generation and maintenance of MCS B, as suggested by Barthlott and Davolio (2015).  
34  
35  
36  
37  
38  
39  
40  
41  
42  
43  
44  
45  
46  
47  
48  
49  
50  
51  
52  
53  
54  
55  
56  
57  
58  
59  
60

1 After **P2**, dry air masses (as revealed from SEVIRI 6.2  $\mu\text{m}$  BTs, e.g. at 0600 UTC, Fig. 11b)  
2 associated with the upper-level trough progressing eastward together with the low-level mistral flow  
3 reached SI, leading to environmental conditions detrimental to deep convection.

## 4 5 **6. Summary**

6 During IOP 13 (15–16 October 2012) of the HyMeX SOP 1, SI experienced two periods of intense  
7 rainfall. The first between 1300 UTC and 1700 UTC on 15 October (period **P1**, maximum hourly  
8 precipitation of  $34.8 \text{ mm h}^{-1}$ ; total precipitation of 62.4 mm), and the second between 2300 and 0200  
9 UTC on 15-16 October (period **P2**, maximum hourly precipitation of  $33.8 \text{ mm h}^{-1}$ ; total precipitation  
10 of 75 mm). The HPEs were both associated with multicell V-shaped retrograde regeneration MCSs  
11 which formed over the Tyrrhenian Sea (responsible for **P1**) and over Tunisia (responsible for **P2**). The  
12 life cycle of the two MCSs in connection with their dynamic and thermodynamic environments were  
13 analysed using a combination of ground-based, airborne and spaceborne observations as well as NWP  
14 model analyses. The main findings are summarized in schematic illustrations shown Fig. 13.

15 MCS A was triggered by low-level convergence (hatched area in Fig. 13a) between the low-  
16 level south-westerly flow ahead of an upper-level trough positioned over south-eastern France and  
17 very-moist low-level south-southwesterly flow from the strait of Sicily. During **P1**, the convection  
18 was favoured by high CAPE values (greater than  $1500 \text{ J kg}^{-1}$ ) over the Tyrrhenian Sea resulting from  
19 moist conditions in the low-levels (water vapor mixing ratio of  $\sim 12 \text{ g kg}^{-1}$  in the lower 1 km of the  
20 MABL). Moreover the presence of an elevated moisture plume from tropical Africa contributed about  
21 one quarter of the large observed TIWV ( $\sim 35 \text{ kg m}^{-2}$ ). After the initiation phase, the V-shaped MCS  
22 moved eastward but remained over the southern Tyrrhenian Sea. According to SEVIRI observations,  
23 it lasted for more than 14 h.

24 Heavy precipitation during **P2** was caused by a MCS initiated over Algeria around 1300 UTC,  
25 which subsequently moved over the Strait of Sicily toward Sicily and SI. Convection was favoured by  
26 the combination of the large low-level moisture contents, an elevated moisture supply (the tropical  
27 plume being associated with a strong southwesterly flow ahead of an eastward-moving upper-level

1  
2  
3  
4 1 trough) and high SSTs in the Sicily Channel ( $\sim 23^{\circ}\text{C}$ ) as well as by a marked wind shear ahead of the  
5  
6 2 front (Fig. 13b). Unlike other MCSs forming in the same region earlier on that day, the huge V-shape  
7  
8 3 system did affect SI because the strong flow ahead of the upper-level trough progressively veered  
9  
10 4 from southwesterly to south-southwesterly thereby guiding the MCS towards SI. The penetration of  
11  
12 5 the mistral in the Strait of Sicily at the end of 15 October (dashed line Fig. 13b) terminated the  
13  
14 6 convective activity west of Sicily. Ultimately, dry air masses associated with low-level mistral and the  
15  
16 7 upper-level trough overpassed SI, terminating the HPE over SI during IOP 13.

17  
18 8 Using as much of the available data as possible in combination with numerical simulations, we  
19  
20 9 show the importance of the southerly flow from the warmer Mediterranean south of Sicily in enhancing the  
21  
22 10 convergence ahead of the large-scale cold front and feeding moisture into the developing MCSs upstream  
23  
24 11 of SI. We also detail the initiation and maintenance processes for MCSs occurring along the previously  
25  
26 12 identified autumnal convective arc between Tunisia, Sicily and SI which appears to be a prominent area of  
27  
28 13 initiation of MCSs leading to HPEs over SI as shown by others (e.g. Funatsu et al., 2009). Furthermore, we  
29  
30 14 highlight the role of the upper-level trough over southern France in organizing convection along the  
31  
32 15 autumnal convective arc. These results suggest that in order to improve model forecasts of the MCSs along  
33  
34 16 this autumnal convection arc as well as HPEs over Sicily and SI, the simulation domain needs to include  
35  
36 17 northern Africa and part of the Eastern Mediterranean Basin.

37  
38 18 As stated in Barthlott and Davolio (2015), it is very difficult for NWP models to simulate accurately  
39  
40 19 the triggering of isolated convection systems (such as MCS A), which are usually associated with low  
41  
42 20 intrinsic predictability. On the other hand, MCS B, that develops later in the evening and is triggered  
43  
44 21 directly by the frontal passage, is better described in their model simulations. Complementary  
45  
46 22 investigations of the HPEs occurring over SI during IOP 13 will be conducted with a high resolution  
47  
48 23 model to enhance our comprehension of the impact of elevated moisture transport from tropical Africa  
49  
50 24 and of the dry air masses observed north of MCS A on the development of deep convection upstream  
51  
52 25 of SI. In addition, sensitivity experiments will be also used to determine whether the rainfall observed  
53  
54 26 during P2 over the southern Italy is of convective or stratiform nature.

55  
56 27

## 1 Acknowledgements

2 This work was supported by the French Agence Nationale de la Recherche (ANR) via the IODA-  
3 MED Grant ANR-11-BS56-0005, the MUSIC grant ANR-14-CE01-014 and the MISTRALS/HyMeX  
4 programme. Airborne data was obtained using the ATR-42 Environment Research Aircraft operated  
5 and managed by Service des Avions Français Instrumentés pour la Recherche en Environnement  
6 (SAFIRE), which is a joint entity of CNRS, Météo-France & CNES (<http://www.safire.fr>). The  
7 SAFIRE staff is thanked for their support during the SOP 1. The authors are grateful to D. Bruneau, P.  
8 Genau, C. Merlet, R. Meynadier, T. Deleporte, S. Bastin, C. Kocha, C. Lavaysse (LATMOS) as well  
9 as F. Blouzon and A. Abchiche (DT/INSU) for operating the LEANDRE 2 system aboard the ATR-42  
10 during the HyMeX-SOP 1. The authors would also like to thank I. Taupier-Letage (MIO) for  
11 discussions and O. Bock (IGN) for the GPS data. The authors warmly thank Dr P. Rosenberg (School  
12 of Earth and Environment, University of Leeds) for his support in improving the English of the paper.  
13 Finally, the authors are grateful to the three anonymous referees whose comments helped improved  
14 the paper significantly. LEANDRE 2 data are available from the HyMeX Database:  
15 [http://dx.doi.org/10.6096/HYMEX.WATER\\_VAPOUR\\_DIAL\\_LEANDRE2.V1.20120911](http://dx.doi.org/10.6096/HYMEX.WATER_VAPOUR_DIAL_LEANDRE2.V1.20120911). AROME-  
16 WMED analyses are also available from the HyMeX database:  
17 [http://dx.doi.org/10.6096/HYMEX.AROME\\_WMED.2012.02.20](http://dx.doi.org/10.6096/HYMEX.AROME_WMED.2012.02.20).

## 19 References

- 20 Barthlott C, Davolio S. 2015. Mechanisms initiating heavy precipitation over Italy during the HyMeX  
21 Special Observation Period 1: A numerical case study using two mesoscale models. *Q. J. R.*  
22 *Meteorol. Soc.* DOI: 10.1002/qj.2630.
- 23 Barthlott C, Adler B, Kalthoff N, Handwerker J, Johler M, Wieser A. 2014. The role of Corsica in  
24 initiating nocturnal offshore convection. *Q. J. R. Meteorol. Soc.* doi: 10.1002/qj.2415.
- 25 Bedka K, Brunner J, Dworak R, Feltz W, Otkin J, Greenwald T. 2009. Objective satellite-based  
26 detection of overshooting tops using infrared window channel brightness temperature gradients.  
27 *J. Appl. Meteorol. Climatol.* **49**: 181–202.

- 1  
2  
3  
4 1 Bedka K. 2011. Overshooting cloud top detections using MSG SEVIRI Infrared brightness  
5  
6 2 temperatures and their relationship to severe weather over Europe. *Atmos. Res.* **99**: 175–189.  
7  
8 3 doi: 10.1016/j. atmosres.2010.10.001.  
9  
10 4 Bock O, Bossler P, Pacione R, Nuret M, Fourrié N, Parracho A. 2015. A high quality reprocessed  
11  
12 5 ground-based GPS dataset for atmospheric process studies, radiosonde and model evaluation,  
13  
14 6 and reanalysis of HyMeX special observing period. *Q. J. R. Meteorol. Soc.*  
15  
16 7 doi :10.1001/qj.2701.  
17  
18 8 Brousseau P, Bouttier F, Hello G, Seity Y, Fischer C, Berre L, Montmerle T, Auger L, Malardel S.  
19  
20 9 2008. A prototype convective-scale data assimilation system for operation: The AROME-RUC.  
21  
22 10 *HIRLAM Tech. Rep.* **68**: 23–30.  
23  
24 11 Browning KA. 1986. Conceptual models of precipitation systems. *Wea. Forecasting*, **1**: 23–41.  
25  
26 12 Bruneau D, Quaglia P, Flamant C, Meissonnier M, Pelon J. 2001a. Airborne Lidar LEANDRE 2 for  
27  
28 13 water vapour profiling in the Troposphere. System description. *Appl. Opt.* **40**: 3450–3461.  
29  
30 14 Bruneau D, Quaglia P, Flamant C, Pelon J. 2001b. Airborne Lidar LEANDRE 2 for water vapour  
31  
32 15 profiling in the Troposphere. First results. *Appl. Opt.* **40**: 3462–3475.  
33  
34 16 Campins J, Genovés A, Jansa A, Guijarro JA, Ramis C. 2000. A catalogue and a classification of  
35  
36 17 surface cyclones for the western Mediterranean. *Int. J. Climatol.* **20**: 969–984.  
37  
38 18 Cailleau S, Chanut J, Lellouche JM, Levier B, Maraldi C, Reffray G, Sotillo MG. 2012. Towards a  
39  
40 19 regional ocean forecasting system for the IBI (Iberia-Biscay-Ireland area): developments and  
41  
42 20 improvements withing the ECOOP project framework. *Ocean Sci.* **8**: 143–159, doi:10.5194/os-  
43  
44 21 8-143-2012.  
45  
46 22 Chazette P, Flamant C, Shang X, Totems J, Raut JC, Doerenbecher A, Ducrocq V, Fourrié N, Bock O,  
47  
48 23 Cloché S. 2015a. A multi-instrument and multi-model assessment of atmospheric moisture  
49  
50 24 variability over the western Mediterranean during HyMeX. *Q. J. R. Meteorol. Soc.*  
51  
52 25 doi:10.1002/qj.2671.  
53  
54 26 Chazette P, Flamant C, Raut JC, Totems J, Shang X. 2015b. Tropical moisture enriched storm tracks  
55  
56 27 over the Mediterranean and their link with intense rainfall in the Cevennes-Vivarais area during  
57  
58  
59  
60

- 1 HyMeX. *Q. J. R. Meteorol. Soc.* doi:10.1002/qj.2674.
- 2 Cohuet JB, Romero R, Homar V, Ducrocq V, Ramis C. 2011. Initiation of a severe thunderstorm over  
3 the Mediterranean Sea. *Atmos. Res.* **100**: 603–620.
- 4 Courtier P, Freyrier C, Geleyn JF, Rabier F, Rochas M. 1991. The ARPEGE project at Meteo-France,  
5 ECMWF workshop on numerical methods in atmospheric modelling, **2**: 193–231.
- 6 Di Girolamo P, Flamant C, Cacciani M, Richard E, Ducrocq V, Summa D, Stelitano D, Fourrié N,  
7 Said F. 2016. Observation of low-level wind reversals in the Gulf of Lion area and their impact  
8 on the water vapour variability, *Q. J. R. Meteorol. Soc.* doi:10.1002/qj.2767.
- 9 Drobinski P, Ducrocq V, Alpert P, Anagnostou E, Béranger K, Borga M, Braud I, Chanzy A, Davolio S,  
10 Delrieu G, Estournel C, Boubrahmi NF, Font J, Grubisic V, Gauldi S, Homar V, Ivancan-Picek  
11 B, Kottmeier C, Kotroni V, Lagouvardos K, Lionello P, Llasat M, Ludwig W, Lutoff C, Mariotti  
12 A, Richard E, Romero R, Rotunno R, Roussot O, Ruin I, Somot S, Taupier-Letage I, Tintore J,  
13 Uijlenhoet R, Wernli H. 2014. HyMeX, a 10 year multidisciplinary program on the  
14 Mediterranean water cycle, *BAMS*, **95**: 1063–1082.
- 15 Drobinski P, Bastin S, Guénard V, Caccia JL, Dabas AM, Delville P, Protat A, Reitebuch O, Werner C.  
16 2005. Summer Mistral at the exit of the Rhône Valley. *Q. J. R. Meteorol. Soc.* **131**: 353–375.
- 17 Ducrocq V, Braud I, Davolio S, Ferretti R, Flamant C, Jansa A, Kalthoff N, Richard E, Taupier-Letage  
18 I, Ayrat PA, Belamari S, Berne A, Borga M, Boudevillain B, Bock O, Boichard JL, Bouin MN,  
19 Bousquet O, Bouvier C, Chiggiato J, Ciimini D, Corsmeier U, Coppola L, Cocquerez P, Defer  
20 E, Delanoë J, Di Girolamo P, Doerenbecher A, Drobinski P, Dufournet Y, Fourrié N, Gourley JJ,  
21 Labatut L, Lambert D, Le Coz J, Marzano FS, Molinié G, Montani A, Nord G, Nuret M,  
22 Ramage K, Rison W, Roussot O, Said F, Schwarzenboeck A, Testor P, Van Baelen J, Vincendon  
23 B, Aran M, Tamayo J. 2014. HyMeX-SOP1: The Field Campaign Dedicated to Heavy  
24 Precipitation and Flash Flooding in the Northwestern Mediterranean. *Bull. Am. Meteorol. Soc.*  
25 **95**: 1083–1100. doi:10.1175/BAMS-D-12-00244.1.
- 26 Duffourg F, Nuissier O, Ducrocq V, Flamant C, Chazette P, Delanoë J, Doerenbecher A, Fourrié N,  
27 Girolamo Di P, Lac C, Legain D, Martinet M, Saïd F, Bock O. 2016. Offshore deep convection

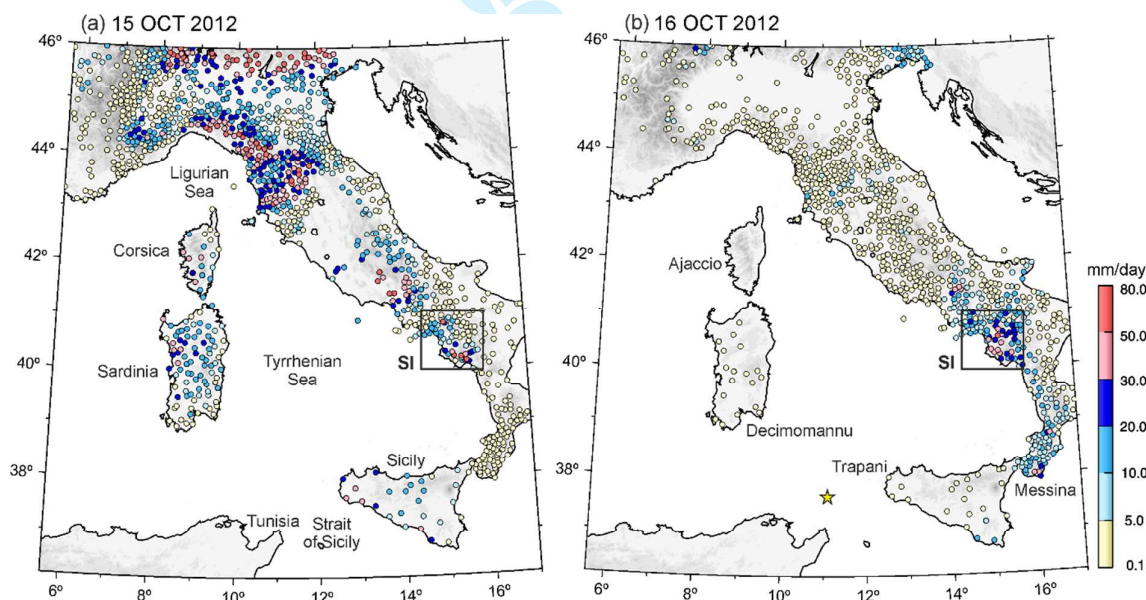
- 1  
2  
3  
4 1 initiation and maintenance during HyMeX IOP 16a heavy precipitation event. *Q. J. R. Meteorol.*  
5  
6 2 *Soc.* doi:10.1002/qj.2725.  
7  
8 3 Duffourg F, Ducrocq V. 2013. Assessment of the water supply to Mediterranean heavy precipitation: A  
9  
10 4 method based on finely designed water budgets. *Atmos. Sci. Lett.* **14**: 133–138.  
11  
12 5 Flamant C, Chaboureaux JP, Chazette P, Di Girolamo P, Bourianne T, Totems J, Cacciani M. 2015. The  
13  
14 6 radiative impact of desert dust on orographic rain in the Cevennes-Vivarais area: a case study  
15  
16 7 from HyMeX, *Atmos. Chem Phys.* **15**: 12231–12249.  
17  
18 8 Flaounas E, Kotroni V, Lagouvardos K, Claud C, Delanoë J, Flamant C, Madonna E, Wernli H. 2015.  
19  
20 9 Processes leading to heavy precipitation associated with two Mediterranean cyclones observed  
21  
22 10 during the HyMeX SOP1. *Q. J. R. Meteorol. Soc.* doi:10.1002/qj.2618.  
23  
24 11 Fourrié N, Bresson E, Nuret M, Jany C, Brousseau P, Doerenbecher A, Kreitz M, Nuissier O, Sevault  
25  
26 12 E, Bénichou H, Amodei M, Pouponneau F. 2015. Arome-wmed, a real-time mesoscale model  
27  
28 13 designed for the HyMeX special observation periods. *Geosci. Model Dev.* **8** (2): 1801–1856.  
29  
30 14 doi:10.5194/gmdd-8-1801-2015.  
31  
32 15 Funatsu B, Claud MC, Chaboureaux JP. 2009. Comparison between the Large-Scale Environments of  
33  
34 16 Moderate and Intense Precipitating Systems in the Mediterranean Region, *Mon. Wea. Rev.*, **137**:  
35  
36 17 3933–3959.  
37  
38 18 Jansa A, 1987. Distribution of the Mistral: A satellite observation. *Meteor. Atmos. Phys.* **36**: 201–214.  
39  
40 19 doi: 10.1007/BF01045149.  
41  
42 20 Jansa A, Genoves A, Picornell MA, Campins J, Riosalido R, Carretero O. 2001. Western  
43  
44 21 Mediterranean cyclones and heavy rain. Part 2: Statistical approach. *Meteorol. Appl.* **8**: 43–56.  
45  
46 22 doi:10.1017/S1350482701001049.  
47  
48 23 Kato T. 2006. Structure of the band-shaped precipitation system inducing the heavy rainfall observed  
49  
50 24 over northern Kyushu, Japan on 29 June 1999. *J. Meteor. Soc. Japan.* **84**(1): 129–153.  
51  
52 25 Kotroni V, Lagouvardos K. 2008. Lightning occurrence in relation with elevation, terrain slope and  
53  
54 26 vegetation cover over the Mediterranean. *J. Geophys. Res.* doi:10.1029/2008JD010605.  
55  
56 27 Lerach DG, Cotton WR. 2012. Comparing aerosol and low-level moisture influences on supercell  
57  
58  
59  
60

- 1  
2  
3  
4 1 tornadogenesis: three-dimensional idealized simulations. *J. Atmos. Sci.* **69**: 969–987.
- 5  
6 2 Lin YL, Chiao S, Wang TA, Kaplan ML, Weglarz RP. 2001. Some common ingredients for heavy  
7  
8 3 orographic rainfall. *Wea. Forecasting*, **16**: 633–660.
- 9  
10 4 Llasat MC, Llasat-Botija M, Petrucci O, Pasqua AA, Rosselló J, Vinet F, Boissier L. 2013. Towards a  
11  
12 5 database on societal impact of mediterranean floods within the framework of the HyMeX project.  
13  
14 6 *Nat. Hazard Earth Sys.* **13(5)**: 1337–1350, doi:10.5194/nhess-13-1337-2013.
- 15  
16 7 Masson V, Seity Y. 2009. Including Atmospheric Layers in Vegetation and Urban Offline Surface  
17  
18 8 Schemes, *J. Appl. Meteorol. Clim.* **48**: 1377–1397.
- 19  
20 9 Masson V, Le Moigne P, Martin E, Faroux S, Alias A, Alkama R, Belamari S, Bardu A, Boone A,  
21  
22 10 Bouyssel F, Brousseau P, Brun E, Calvet JC, Carrer D, Decharme B, Delire C, Donier S,  
23  
24 11 Essauouini K, Gibelin AL, Giordani H, Habets F, Jidane M, Kerdraon G, Kourzeneva E,  
25  
26 12 Lafaysse M, Lafont S, Lebeaupin BC, Lemonsu A, Mahfouf JF, Marguinaud P, Mokhtari M,  
27  
28 13 Morin S, Pigeon G, Salgado R, Seity Y, Taillefer F, Tanguy G, Tulet P, Vincendon B, Vionnet  
29  
30 14 V, Voltaire A. 2013. The surfex v7.2 land and ocean surface platform for coupled or offline  
31  
32 15 simulation of earth surface variables and fluxes. *Geosci. Model Dev.* **6(4)**: 929–960,  
33  
34 16 doi:10.5194/gmd-6-929-2013.
- 35  
36 17 Mc Cann DW. 1983. The enhanced-V: a satellite observable severe storm signature. *Mon. Wea. Rev.*,  
37  
38 18 **111**: 887–894.
- 39  
40 19 Melani S, Pasi F, Gozzini B, Ortolani A. 2013. A four year (2007–2010) analysis of long-lasting deep  
41  
42 20 convective systems in the Mediterranean basin. *Atmos. Res.*, **123**: 151–166.
- 43  
44 21 Nuissier O, Ducrocq V, Ricard D, Lebeaupin C, Anquetin S. 2008. A numerical study of three  
45  
46 22 catastrophic precipitating events over southern France. I: Numerical framework and synoptic  
47  
48 23 ingredients. *Q. J. R. Meteorol. Soc.* **134**: 111–130.
- 49  
50 24 Nuissier P, Joly B, Joly A, Ducrocq V, Arbogast P. 2011. A statistical downscaling to identify the  
51  
52 25 large-scale circulation patterns associated with heavy precipitation events over southern France.  
53  
54 26 *Q. J. R. Meteorol. Soc.* **137**: 1812–1827. doi:10.1002/qj.866.
- 55  
56 27 Ricard D, Ducrocq V, Auger L. 2012. A climatology of the mesoscale environment associated with  
57  
58  
59  
60



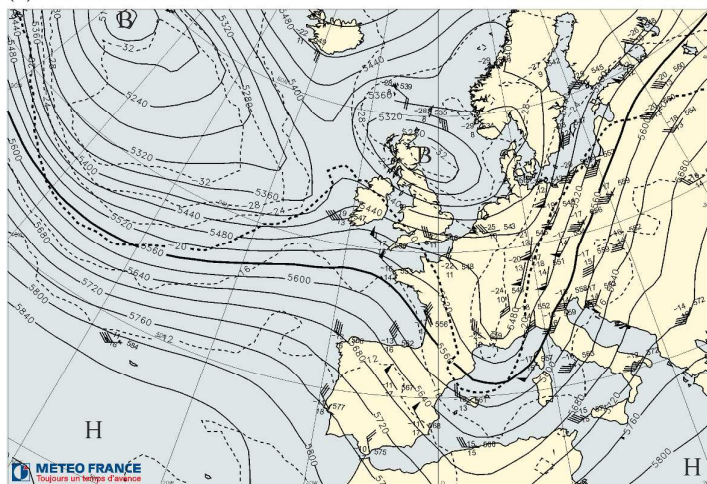
- 1  
2  
3  
4 1 heavily precipitating events over a northwestern mediterranean area. *J. Appl. Meteorol.*  
5  
6 2 *Climatol.* **51**: 468–488. doi:10.1175/JAMC-D-11-017.1.  
7  
8 3 Rivrain JC. 1997. Les épisodes orageux à précipitations extrêmes sur les régions méditerranéennes de  
9  
10 4 la France. Phénomènes remarquables n° 4, Météo-France, Toulouse, 93 p.  
11  
12 5 Romero R, Sumner G, Ramis C, Genoves A. 1999. A classification of the atmospheric circulation  
13  
14 6 patterns producing significant daily rainfall in the Spanish Mediterranean area. *Int. J. Climatol.*  
15  
16 7 **19**: 765–785.  
17  
18 8 Romero R, Ramis C, Homar V. 2015. On the severe convective storm of 29th October 2013 in the  
19  
20 9 Balearic Islands: Observational and numerical study. *Q. J. R. Meteorol. Soc.*  
21  
22 10 doi:10.1002/qj.2429.  
23  
24 11 Rotunno R, Ferretti R. 2001. Mechanisms of intense Alpine rainfall. *J. Atmos. Sci.* **58**: 1732–1749.  
25  
26 12 Rotunno R, Houze RA. 2007. Lessons on orographic precipitation from the Mesoscale Alpine  
27  
28 13 Programme. *Q. J. R. Meteor. Soc.* **133**: 811–830.  
29  
30 14 Rysman JF, Claud C, Chaboureau JP, Delanoë J, Funatsu BM. 2015. Severe convection in the  
31  
32 15 Mediterranean from microwave observations and a convection-permitting model. *Q. J. R.*  
33  
34 16 *Meteorol. Soc.* doi:10.1002/qj.2611.  
35  
36 17 Scofield RA. 1985. Satellite convective categories associated with heavy precipitation. Preprints,  
37  
38 18 Sixth Conference on hydrometeorology, October 29, 1985, Indianapolis, *Amer. Meteor. Soc.*,  
39  
40 19 42-51.  
41  
42 20 Seity Y, Brousseau P, Malardel S, Hello G, Bernard P, Bouttier F, Lac C, Masson V. 2011. The  
43  
44 21 AROME-France convective-scale operational model. *Mon. Weather. Rev.* **139**: 976–991,  
45  
46 22 doi:10.1175.2011MWR3425.1.  
47  
48 23 Setvák M, Rabin RM, Wang PK. 2007. Contribution of the MODIS instrument to observations of  
49  
50 24 deep convective storms and stratospheric moisture detection in GOES and MSG imagery.  
51  
52 25 *Atmos. Res.* **83**: 505–518.  
53  
54 26 Trapero L, Bech J, Lorente J. 2013a. Numerical modelling of heavy precipitation events over Eastern  
55  
56 27 Pyrenees: Analysis of orographic effects. *Atmos. Res.* **123**: 368–383.

- 1 Trapero L, Bech J, Duffourg F, Esteban P, Lorente J. 2013b. Mesoscale numerical analysis of the  
 2 historical November 1982 heavy precipitation event over Andorra (Eastern Pyrenees). *Nat.*  
 3 *Hazards Earth Syst. Sci.* **13**: 2969–2990.
- 4 Trigo IF, Davies TD, Bigg GR. 1999. Objective climatology of cyclones in the Mediterranean region.  
 5 *J. Climate*, **12**: 1685–1696.
- 6 Turato B, Reale O, Siccardi F. 2004. Water vapour sources of the October 2000 Piedmont flood. *J.*  
 7 *Hydrometeorol.* **5**: 693–712. doi:10.1175/1525-7541(2004)005<0693:WVSOTO>2.0.CO;2.
- 8 Winschall A, Pfahl S, Sodemann H, Wernli H. 2012. Impact of north Atlantic evaporation hot spots on  
 9 southern Alpine heavy precipitation events. *Q. J. R. Meteorol. Soc.* **138**: 1245–1258.  
 10 doi:10.1002/qj.987.



13  
 14  
 15 **Figure 1.** 24-h accumulated rainfall on (a) 15 October and (b) 16 October 2012. The Southern Italy (SI) domain is shown as  
 16 a black rectangle (from 14.6 to 16.0 °E and from 40.0 to 41.0 °N). A yellow star in (b) indicates the location (around 11.5°E,  
 17 37.5°N) of the buoy measurements acquired during IOP 13 (see text for details).

(a) 500 hPa ANALYSES 1200 UTC 15 OCT 2012



(b) SURFACE ANALYSES 1200 UTC 15 OCT 2012

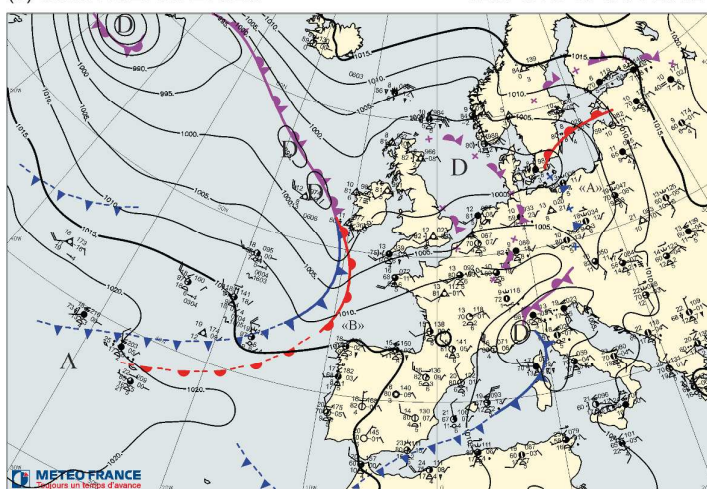
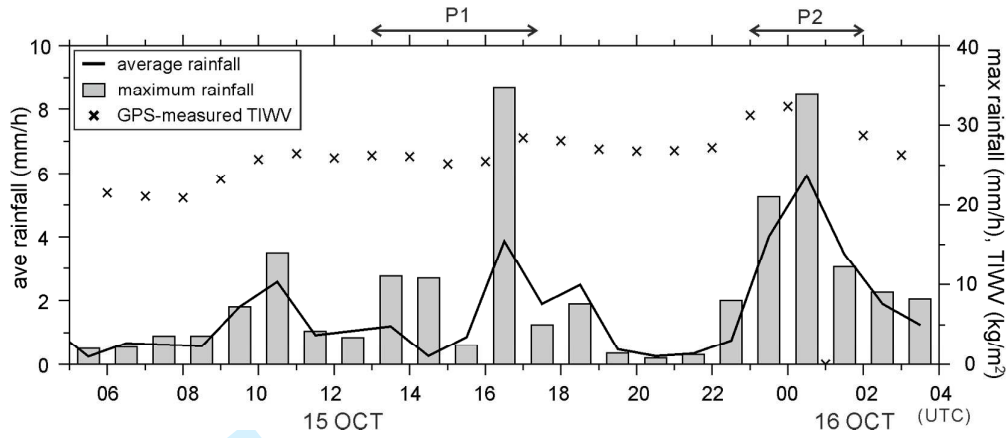


**Figure 2.** Weather charts at 1200 UTC, 15 Oct. 2012. (a) 500 hPa analyses: geopotential height (solid line, 40 m interval) and temperature (dashed line, 4°C interval), and (b) surface analyses: mean sea level pressure (solid line, 5 hPa interval) and fronts (warm fronts in red and cold fronts in blue).



1  
2

3 **Figure 3.** Temporal evolution of observed average hourly rainfall over the SI domain (solid line) and maximum hourly  
 4 rainfall (bar) within SI domain. The temporal evolution of GPS-derived hourly TIWV from a station located at 15.8 °E,  
 5 39.9 °N is also shown (crosses).

17  
18  
19  
20  
21  
22  
23  
24  
25  
26  
27  
28  
29  
30  
31  
32  
33  
34  
35  
36  
37  
38  
39  
40  
41  
42  
43  
44  
45  
46  
47  
48  
49  
50  
51  
52  
53  
54  
55  
56  
57  
58  
59  
60

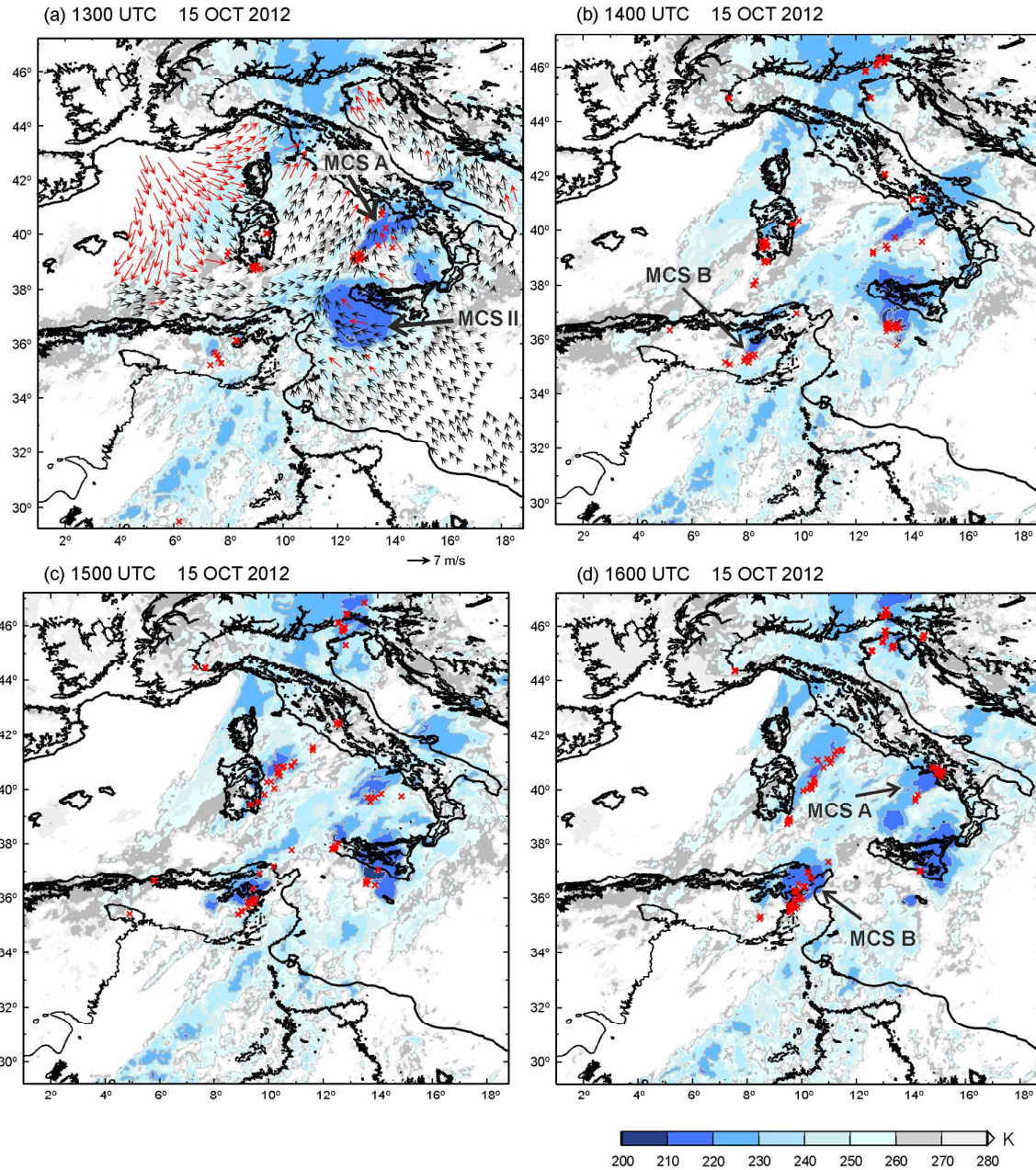
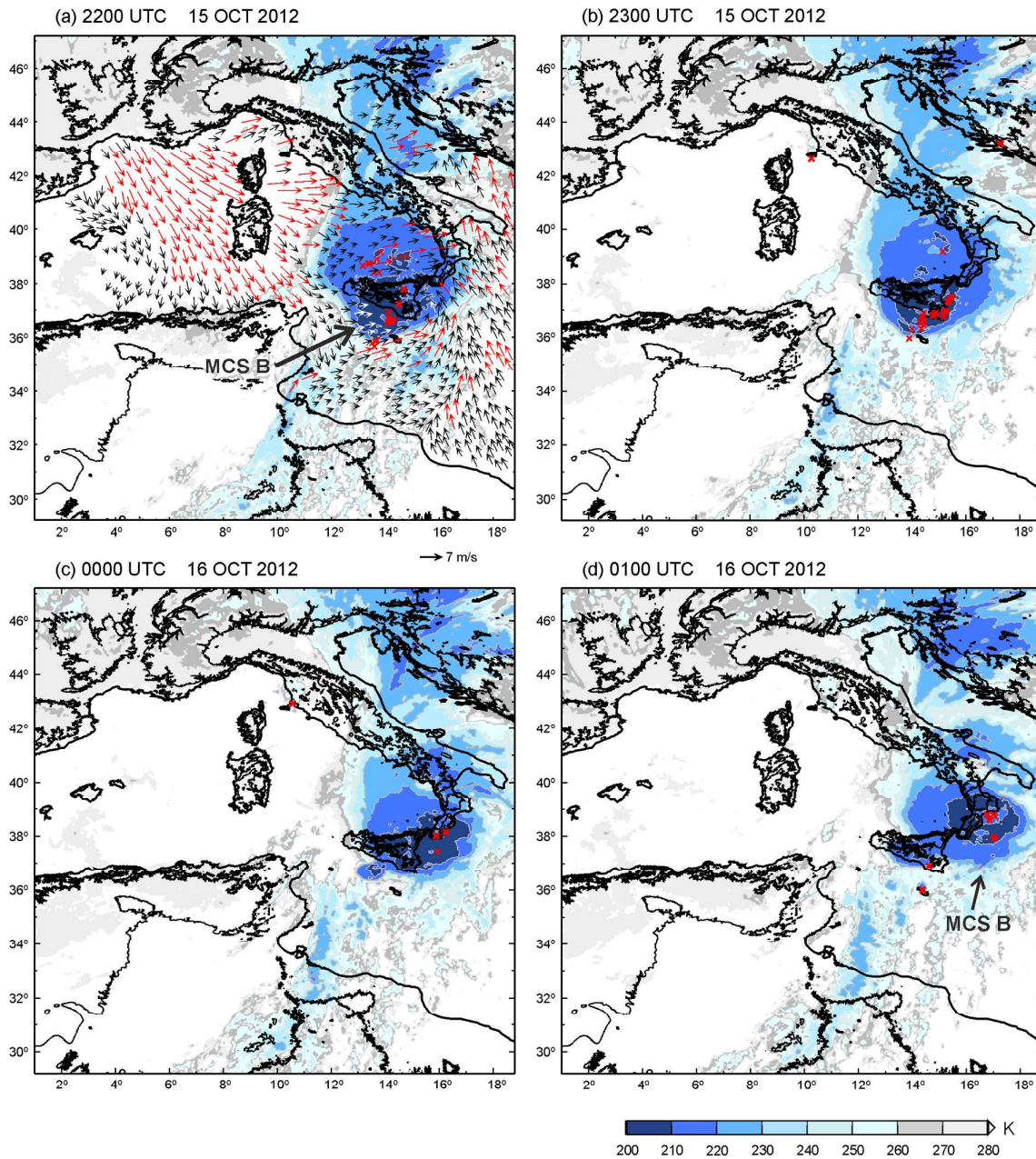


**Figure 4.** Distribution of brightness temperature at 10.8 μm (K) observed with SEVIRI MSG at (a) 1300 UTC, (b) 1400 UTC, (c) 1500 UTC, and (d) 1600 UTC on 15 Oct. 2012. In (a) NOAA OSCAT-retrieved surface winds observed around 1130 UTC are overlaid: red vectors for winds stronger than 10 m s<sup>-1</sup> and black vectors for winds in between 3–10 m s<sup>-1</sup>. Red crosses in (a)–(d) indicate the location of lightning during the 5 minutes preceding the time of SEVIRI imagery. MCS A, MCS B and MCS II are meteorological features of interest (see text for details).



1  
2  
3 **Figure 5.** Same as Fig. 4 but at (a) 2200 UTC, (b) 2300 UTC on 15 Oct. 2012, (c) 0000 UTC and (d) 0100 UTC 16 Oct.  
4 2012. In (a) NOAA OSCAT-retrieved surface winds observed around 2235 UTC are overlaid: red vectors for winds stronger  
5 than  $10 \text{ m s}^{-1}$  and black vectors (white around the region of low BT with the value  $< 210 \text{ K}$ ) for winds between  $3\text{--}10 \text{ m s}^{-1}$ .  
6 MCS B is a meteorological feature of interest (see text for details).

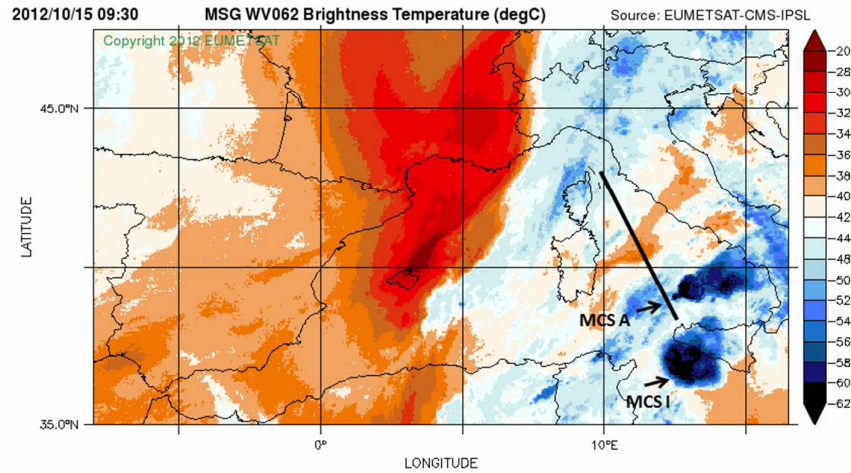
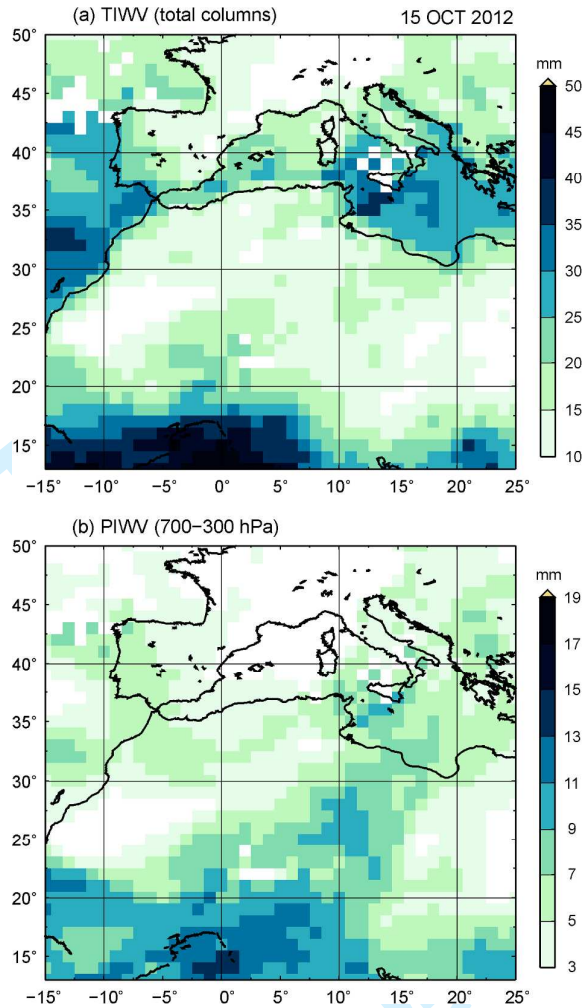


**Figure 6.** Distribution of brightness temperature at 6.2  $\mu\text{m}$  ( $^{\circ}\text{C}$ ) observed by SEVIRI MSG at 0930 UTC, 15 Oct. 2012. The black line indicates the ATR 42 flight track. MCS A and MCS I are meteorological features of interest (see text for details).



1  
2  
3  
4

**Figure 7.** Horizontal distribution of (a) total integrated water vapour content and (b) partial integrated water vapour content between 700 and 300 hPa derived from MODIS/Terra on 15 Oct. 2012.



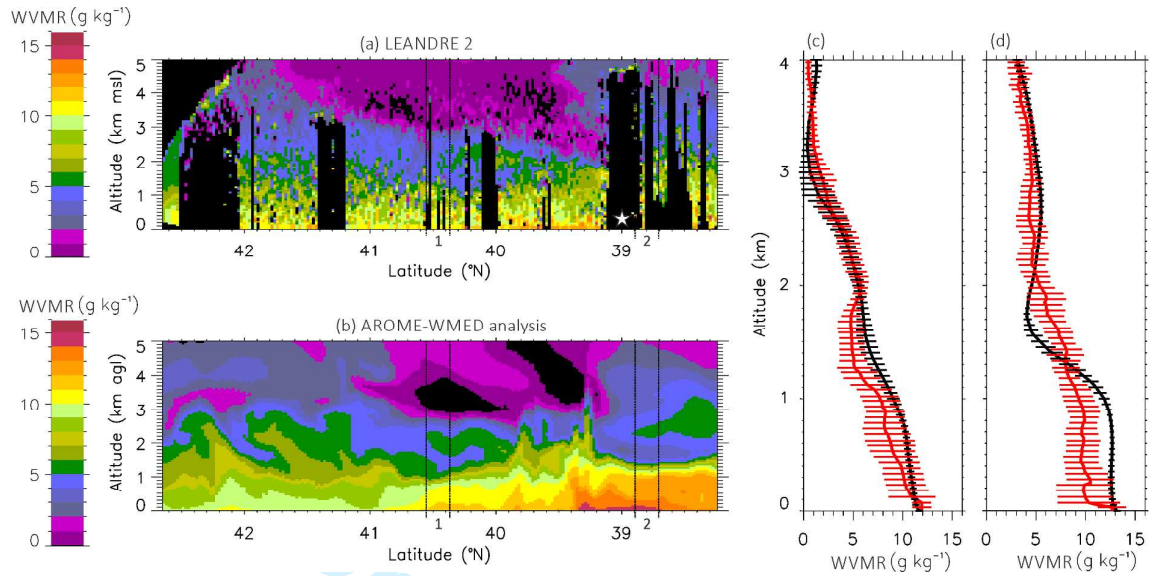


**Figure 8.** (a) Vertical cross-section of water vapour mixing ratio (WVMR) acquired from LEANDRE 2 along the ATR 42 flight track shown in Fig. 6. (b) Same as (a) but for AROME-WMED. WVMR profiles are extracted along the ATR 42 flight track at the closest time and location of the LEANDRE 2 WVMR profiles. (c) Vertical WVMR profiles obtained from LEANDRE 2 (red solid line) and AROME (black solid line) averaged over 60 km (area bracketed by 2 vertical solid lines and marked “1” in (a) and (b)). (d) Same as (c), but for the area in (a) and (b) marked “2”. Horizontal bars in (c) and (d) are an indication of the natural variability of WVMR around the mean profiles. The length of horizontal bars is equal to 2 times the WVMR standard deviation centred on the profiles. The star in (a) marks the latitude (around 39 °N) of MCS A at 0910 UTC.

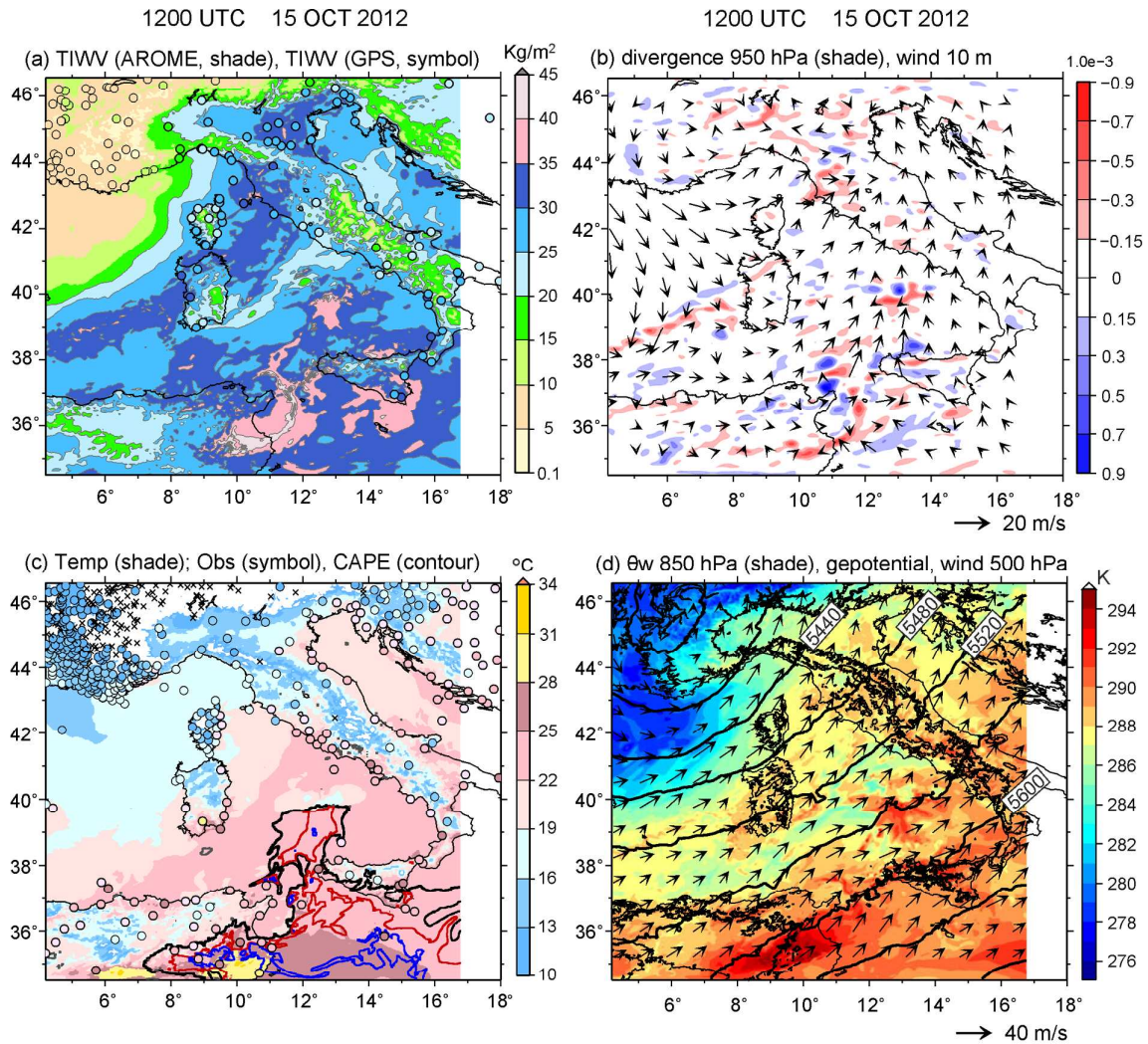


**Figure 9.** Horizontal distribution of (a) TIWV, (b) 950 hPa divergence (shading) and 10 m winds (vectors), (c) 2-m temperature (shading) and CAPE (contours with interval of  $500 \text{ J kg}^{-1}$  from  $1000 \text{ J kg}^{-1}$ ) and (d) 850 hPa pseudo-adiabatic potential temperature ( $\theta_w$ , shading) and 500 hPa geopotential (contour, interval of 40 m) and wind (vectors) from the AROME-WMED analysis at 1200 UTC, 15 Oct. 2012. Open coloured circles in (a) represent GPS-derived TIWV observations at 1200 UTC. Open coloured circles in (c) represent 2-m temperature observations from SYNOP stations at 1200 UTC. Crosses in (c) represent SYNOP 2-m temperatures less than  $10^{\circ}\text{C}$ .

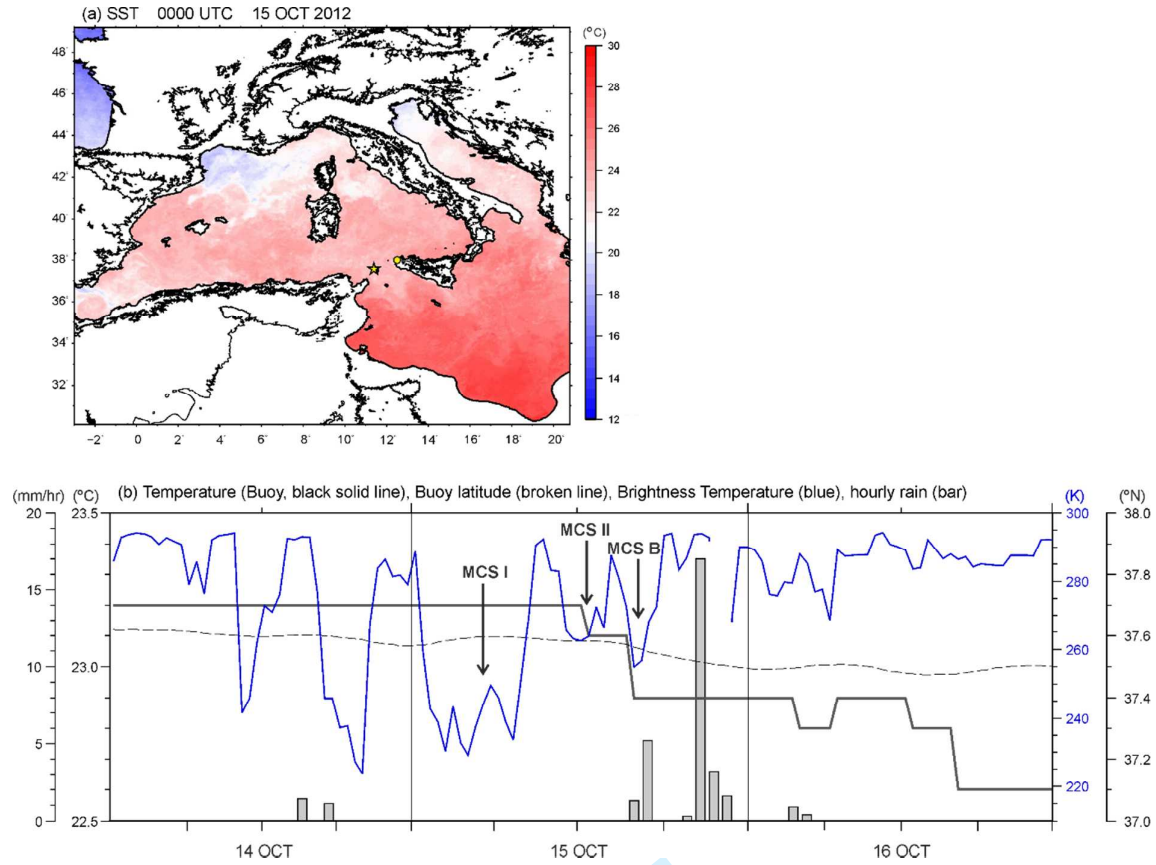
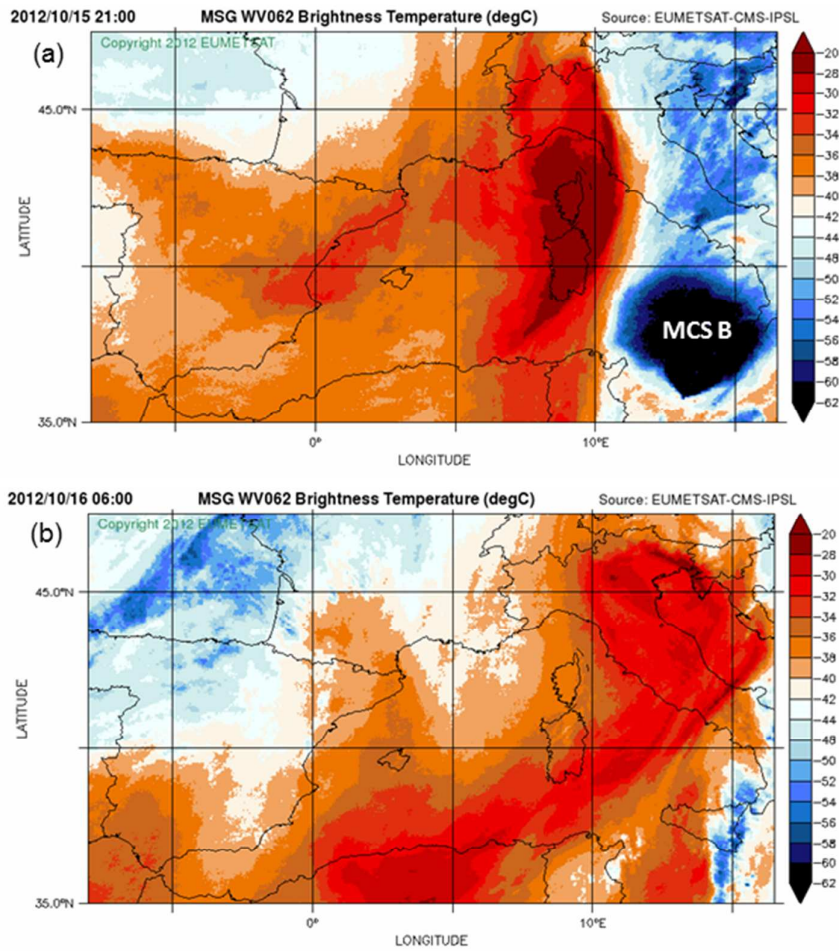


**Figure 10.** (a) SST distribution obtained from CMS multi-sensor (level 3) product at 0000 UTC, 15 Oct. 2012. The yellow star (circle) indicates the location of the buoy (rain gauge) for which data are shown in (b). (b) Time evolution of the buoy location (latitude °N, dashed line) and SST (°C, black solid line) measured by the buoy between 0000 UTC, 14 Oct. and 0000 UTC, 17 Oct. 2012. The blue solid line represents the SEVIRI 10.8 μm brightness temperature (K) extracted at the location of the buoy. Hourly rainfall amount (mm h<sup>-1</sup>) observed by the rain gauge located at 12.5°E, 38 °N are shown as grey bars.



1  
2  
3  
4  
5

**Figure 11.** Distributions of brightness temperature at 6.2 μm (°C) observed by SEVIRI (a) at 2100 UTC, 15 Oct. 2012, and (b) at 0600 UTC, 16 Oct. 2012.

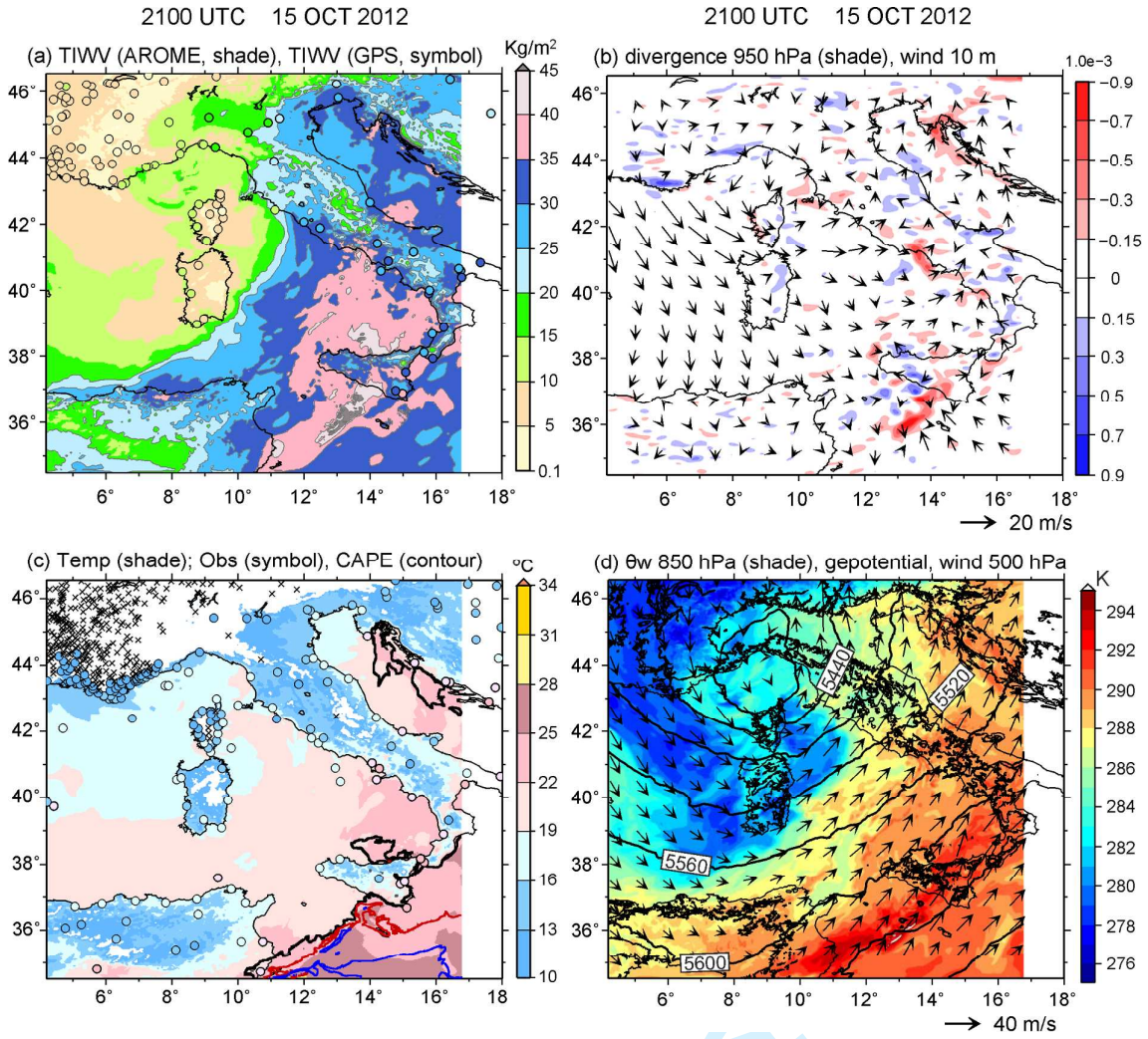
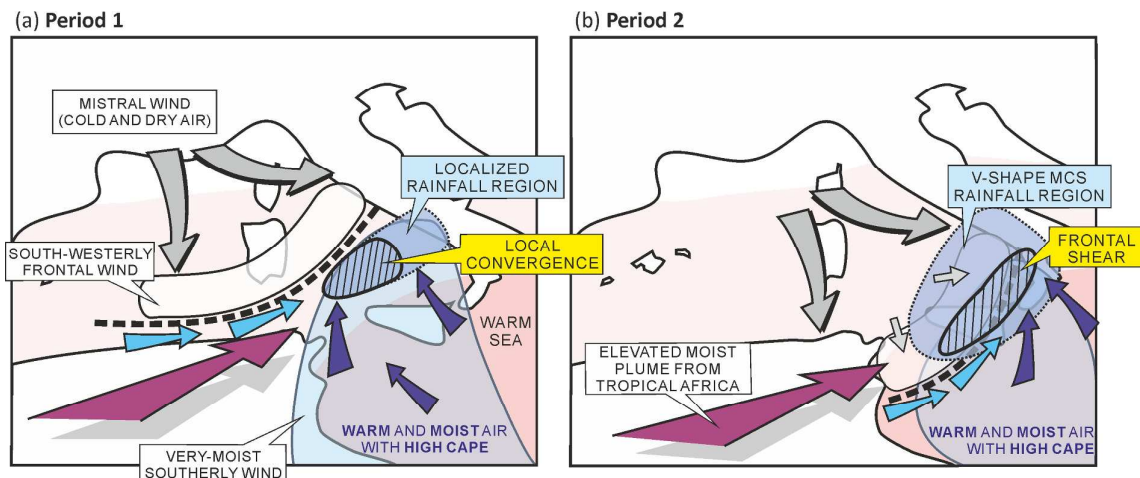


Figure 12. Same as Fig. 9 but for 2100 UTC, 15 Oct. 2012.



1  
2  
3  
4  
5  
6  
7  
8  
9  
10  
11  
12  
13  
14  
15  
16  
17  
18  
19  
20  
21  
22  
23  
24  
25  
26  
27  
28  
29  
30  
31  
32  
33  
34  
35  
36  
37  
38  
39  
40  
41  
42  
43  
44  
45  
46  
47  
48  
49  
50  
51  
52  
53  
54  
55  
56  
57  
58  
59  
60

**Figure 13.** Schematics summarizing the main features and processes responsible for the maintenance of deep convection upstream of SI and leading to HPEs for Period 1 (a) and Period 2 (b). In (a) and (b), grey arrows indicate the mistral wind behind the edge of the cold front (thick dashed line). The white-shaded area enclosed in the black solid line represents the high TIWV region just north of the front. The light blue arrows depict the low-level westerlies to south-westerlies ahead of the front. Dark blue arrows show the low-level moist southerlies from the Eastern Mediterranean encompassed in the blue-shaded area. The purple arrow illustrates the elevated tropical plume. The local low-level convergence during P1 and the frontal shear during P2 are indicated by a hatched areas in (a) and (b), respectively. The rainfall regions are indicated by blue-shaded encapsulated with the dotted line.